Monthly Notices of the ROYAL ASTRONOMICAL SOCIETY

MNRAS **543,** 4218–4234 (2025) https://doi.org/10.1093/mnras/staf1684
Advance Access publication 2025 October 3

Modelling multiwavelength afterglows of the VHE-GRB population

Monica Barnard [1,2,5★] Ankur Ghosh [1★] Jagdish C. Joshi[1,3] and Soebur Razzaque [1,4,5★]

[1]*Centre for Astro-Particle Physics (CAPP) and Department of Physics, University of Johannesburg, PO Box 524, Auckland Park 2006, South Africa*
[2]*Centre for Space Research, North-West University, Private Bag X6001, Potchefstroom 2520, South Africa*
[3]*Aryabhatta Research Institute of Observational Sciences, Manora Peak, Nainital 263129, India*
[4]*Department of Physics, The George Washington University, Washington, DC 20052, USA*
[5]*National Institute for Theoretical and Computational Sciences (NITheCS), Private Bag X1, Matieland, South Africa*

Accepted 2025 September 29. Received 2025 September 24; in original form 2025 May 30

ABSTRACT

The recent detection of very high energy (VHE, $\gtrsim$100 GeV) gamma-ray emission from gamma-ray bursts (GRBs) has provided new insights into afterglow physics. Understanding the temporal and spectral evolution of VHE GRBs requires detailed modelling of multiwavelength observations spanning radio to VHE gamma-rays. Previous studies interpreted afterglow of VHE GRBs using a range of frameworks, including single- and multizone jet configurations, synchrotron radiation from forward and reverse shocks, synchrotron self-Compton (SSC) processes, as well as hadronic emission processes. We have modelled five long-duration VHE GRBs – GRB 180720B, GRB 190114C, GRB 190829A, GRB 201216C, and GRB 221009A; using the NAIMA code and modifications to it. The results from our analysis indicate that SSC is the dominant VHE emission mechanism, with negligible contribution from external Compton. Most VHE GRBs are well described by the forward shock model in a spherical jet configuration, where constant density interstellar medium is preferred over wind medium. Additionally, we find that VHE GRBs tend to occur in environments with lower magnetic fields and higher ambient medium densities. Interestingly, VHE GRBs lie at the edge of the 3σ region of the $E_{\rm k,iso}$–ϵ_B correlation observed in other energetic GRBs. Our model slightly over predicts the radio fluxes, indicating that a more complicated modelling might be required in some cases. These findings provide crucial constraints on VHE GRB emission sites and mechanisms and serve as a benchmark for future observations and theoretical studies in the era of CTA and next-generation gamma-ray observatories.

Key words: radiation mechanisms: non-thermal – (stars:) gamma-ray burst: general.

1 INTRODUCTION

The detection of very high energy (VHE, $\gtrsim$100 GeV) gamma-rays from gamma-ray bursts (GRBs) provided us a distinct emission component to investigate particle acceleration and radiation, as well as the properties of ultra-relativistic jets and the surrounding environment. VHE photons have been detected mainly during the afterglow phase of GRBs (see e.g. A. Berti & A. Carosi 2022; R. Gill & J. Granot 2022; D. Miceli & L. Nava 2022), and could be an extension of the late-time GeV emission (see e.g. M. Ackermann et al. 2013; N. Gehrels & S. Razzaque 2013; M. Ajello et al. 2019). The afterglow phase begins, following the prompt emission in MeV, as the jet interacts with the surrounding medium, producing external shocks. These shocks accelerate particles and amplify magnetic fields (B-fields), leading to multiwavelength radiation, analysing which can provide crucial information about energy release, jet structure and composition, and the surrounding environment of these bursts (see e.g. T. Piran 2004; P. Mészáros 2006; P. Kumar & B. Zhang 2015).

Currently, VHE gamma-ray afterglow emission has been detected from six long-duration GRBs, including GRB 180720B (H. Abdalla et al. 2019), GRB 190114C (MAGIC Collaboration 2019a), GRB 190829A (H. Abdalla & others 2021), GRB 221009A (The LHAASO Collaboration 2023), GRB 201015A (O. Blanch et al. 2020), and GRB 201216C (H. Abe et al. 2024). Detection of VHE emission from a short burst, GRB 160821B, has also been reported at 3σ level (V. A. Acciari et al. 2021). All these discoveries have been made with ground-based gamma-ray detectors such as High Energy Stereoscopic System (H.E.S.S.), Major Atmospheric Gamma Imaging Cherenkov Telescopes (MAGIC), and Large High Altitude Air Shower Observatory (LHAASO). A natural question to ask is the emission mechanism of VHE gamma-rays from these GRBs. Synchrotron radiation by shock-accelerated electrons successfully explains radio, optical, X-ray, and GeV gamma-ray afterglows. However, it is challenging to explain VHE gamma-rays with synchrotron radiation, especially the detection of GRB 190114C in up to $\approx$1 TeV gamma-rays by MAGIC (MAGIC Collaboration 2019a, b), and of GRB 221009A in $\gtrsim$10 TeV gamma-rays by LHAASO (Z. Cao et al. 2023).

The synchrotron self-Compton (SSC) has been explored to predict VHE emission from the afterglow forward shock in the past (see e.g. C. D. Dermer, J. Chiang & K. E. Mitman 2000; A. Panaitescu & P. Kumar 2000; R. Sari & A. A. Esin 2001; E. Nakar, S. Ando & R. Sari 2009). Discovery of VHE emission led to modelling multiwavelength data from GRBs using the synchro-SSC emissions (see e.g. H.

★ E-mail: Monica.Barnard@nwu.ac.za (MB); ghosh.ankur1994@gmail.com (AG); srazzaque@uj.ac.za (SR)

Abdalla et al. 2019; X.-Y. Wang et al. 2019; MAGIC Collaboration 2019a; E. Derishev & T. Piran 2021; N. Fraija et al. 2021; J. C. Joshi & S. Razzaque 2021; O. S. Salafia et al. 2022; S. Yamasaki & T. Piran 2022; M. Klinger et al. 2023). Compton scattering of external radiation fields, such as the cosmic microwave background (CMB) and infrared (IR) backgrounds, has also been considered for modelling the multiwavelength data together with synchrotron and SSC (B. T. Zhang et al. 2021, 2023; M. Barnard, S. Razzaque & J. C. Joshi 2024). Modelling the long-term multiwavelength observations of GRB 190114C by K. Misra et al. (2021) found that the microphysical parameters of the synchro-SSC model may evolve with time. E. Guarini et al. (2023) studied the afterglow properties of GRB 180720B, GRB 190114C, and GRB 221009A and found that these bursts might have occurred in the low-density circumburst medium if the SSC mechanism produces the VHE radiation.

The ultra high-energy protons, if co-accelerated with the electron in GRBs, can radiate VHE synchrotron photons, because of a proton's mass heavier than an electron (T. Totani 1998; S. Razzaque 2010; S. Razzaque, C. D. Dermer & J. D. Finke 2010). This emission mechanism has been investigated in the forward shock (H. Isravel, A. Pe'er & D. Bégué 2023a; H. Isravel, D. Bégué & A. Pe'er 2023b) and in the reverse shock (B. T. Zhang et al. 2023) to model VHE afterglows. Photohadronic interactions by ultra high-energy protons with afterglow photons have also been investigated to model VHE emission from GRBs (S. Sahu & C. E. L. Fortín 2020; S. Sahu, I. A. Valadez Polanco & S. Rajpoot 2022; M. Klinger et al. 2024). It should be noted that the total energy requirement for these models often exceeds the observed gamma-ray energy release. UHE protons, if escaping as cosmic rays, can interact with the CMB and IR backgrounds to produce line-of-sight VHE emission to explain $\gtrsim$10 TeV photons detected by LHAASO from GRB 221009A (R. Alves Batista 2022; S. Das & S. Razzaque 2023; N. Mirabal 2023).

Multizone models with synchro-SSC emissions have also been proposed to model multiwavelength data of GRBs detected with VHE gamma-rays. The most natural of these models is a combination of reverse- and forward-shock emissions used for modelling GRB 180720B data (M. Arimoto et al. 2024). Two-component jet models, i.e. combinations of a narrow and a wider jets (Y. Sato et al. 2021, 2023a, b), or a core and a wing (J. Ren et al. 2023; J.-H. Zheng et al. 2024) or a structured jet (B. O'Connor et al. 2023) have also been used to explain the details of the afterglows in VHE GRBs. A two-zone model having different B-field strengths was developed for GRB 190829A, in which the weaker B-field electrons are scattered by the synchrotron photons available in the stronger B-field to produce an intensity of VHE gamma-rays (D. Khangulyan, A. M. Taylor & F. Aharonian 2023).

In this work, we fit multiwavelength data from the population of VHE GRBs with synchro-Compton emission to the extent of a single-zone, namely the forward shock, scenario. For this purpose, we employ the publicly available NAIMA code (V. Zabalza 2015)[1] with some modifications. Our goal is to exhaustively explore this one-zone scenario by fitting as much broad-band and multi-epoch data as possible for the VHE GRBs. This work, therefore, can identify cases where models with multi-emission zones are necessary.

The outline of this paper is the following. In Section 2, we briefly discuss the afterglow emission model used in our work. In Section 3, we describe the data for each GRB that was analysed and used for fitting. In Section 3.2, we apply the NAIMA code, described in Appendix A, to the aforementioned GRBs and compare our results to the multiwavelength observations, with the discussion following in Section 4. Lastly, the blastwave modelling for different scenarios in the NAIMA code and the Markov chain Monte Carlo (MCMC) technique are described in detail in Appendices A and B.

2 AFTERGLOW EMISSION MODELLING

We perform afterglow modelling in this work with emission from the forward shock of the GRB blastwave after the deceleration time ($t_{\rm dec}$), when it evolves following the self-similar set of equations in either a constant-density interstellar medium (ISM) or in a pre-existing stellar wind of the progenitor star, with density $\propto R^{-2}$ where R is the radius from the star (R. D. Blandford & C. F. McKee 1976). More details on how the evolution of the forward-shock radius and bulk Lorentz factor are implemented in the NAIMA code are given in Appendix A1. In modelling the GRB afterglow emission, NAIMA uses a steady-state approximation for the underlying particle distributions and radiative processes. This approach assumes that the electron population reaches equilibrium on time-scales shorter than or comparable to the dynamical evolution of the blast wave. This simplification is commonly used and captures the general spectral and temporal behaviour of GRB afterglows. We are aware that the steady-state approximation may introduce a systematic uncertainty in the parameter estimates due to the time-dependent nature of the GRB afterglow environment. However, this type of model uncertainty is difficult to quantify and has not been explicitly accounted for in the present analysis. As a result, the reported uncertainties reflect only the statistical errors, and the total error budget may be underestimated. Note also that NAIMA does not calculate $t_{\rm dec}$ or produce light curves, and thus we use equations (1) and (2) from M. Barnard et al. (2024) to estimate the initial Bulk Lorentz factor Γ_0 of the blastwave. We set the $t_{\rm dec} \equiv t_p$ (peak time) or $\equiv T_{90}$ (the time duration for a burst to emit from 5 per cent to 95 per cent of its total measured counts), by studying the afterglow light curves of previous studies, and depending on the longer time duration at which the afterglow emission is expected to occur. The values of t_p and T_{90} are associated with the lab frame, thus we apply a factor $(1+z)$ correction, with z the redshift, to convert these times in the rest frame of the burst. In the wind scenario $A = 3.02 \times 10^{35} A_*$ cm^{-1}, with $A_* \equiv \dot{M}_{\rm w}/v_{\rm w} = \dot{M}_{-5}/v_8$ recorded in Table 1 along with the ISM density n in cm^{-3} (see M. Barnard et al. 2024 for more details).

NAIMA has been developed for modelling of galactic objects, however it has also been extended for the SSC modelling of GRBs.[2] In this code the synchrotron radiation is calculated using the formalism as described by F. A. Aharonian, S. R. Kelner & A. Y. Prosekin (2010) while the inverse Compton (IC) radiation with non-thermal and thermal photons is based on F. A. Aharonian & A. M. Atoyan (1981) and D. Khangulyan, F. A. Aharonian & S. R. Kelner (2014). The details of synchrotron, SSC, and external Compton (EC) emission calculations in NAIMA are discussed in Appendices A3, A4, and A5, respectively. The modification we have made to calculate the maximum electron energy is described in Appendix A6.

In addition to the calculation of emissions, NAIMA also calculates $\gamma\gamma$ attenuation within the emission region. The opacity for the $\gamma\gamma$ attenuation calculation within the emission region follows F. A. Aharonian (2004) and A. Eungwanichayapant & F. Aharonian (2009). The details of the $\gamma\gamma$ attenuation are described in Appendix A7.

[1] Additional documentation on the code and the installation thereof is available at http://naima.readthedocs.org.

[2] https://github.com/Carlor87/GRBmodelling

Table 1. A summary of the model parameter values found that best fit the observations for each combination of GRB and density scenario. Bold values were held fixed during the fitting process, except for Γ_0 and ϵ_B which were calculated based on other parameters (see the main text for details). We assumed $E_{\rm k,iso}$ to be five times the isotropic-equivalent gamma-ray energy release $E_{\gamma,\rm iso}$.

Parameter	180720B		190114C		190829A		201216C		221009A	
	ISM	Wind	ISM	Wind	ISM	Wind	ISM	Wind	ISM	Wind
$E_{\rm k,iso}$ (erg)	6×10^{53}	1×10^{54}	8×10^{53}	8×10^{53}	1×10^{52}	1×10^{52}	6×10^{53}	6×10^{53}	1.5×10^{55}	1.2×10^{55}
Γ_0	246	129	167	107	88	30	362	86	129	100
$t_{\rm dec}$ (s)	78		116		63		60		230	
$\dot{M}_{\rm w}$ ($M_\odot$ yr^{-1})	–	1×10^{-5}	–	1×10^{-5}	–	5×10^{-5}	–	5×10^{-5}	–	8×10^{-5}
$v_{\rm w}$ (cm s^{-1})	–	1×10^{8}	–	1×10^{8}	–	2×10^{8}	–	1×10^{8}	–	1×10^{8}
A_*	–	1	–	1	–	2.5	–	5	–	8
n_0 (cm^{-3})	5×10^{-1}	–	5	–	30	–	1×10^{-1}	–	30	–
ϵ_B	3.5×10^{-3}	2.5×10^{-4}	4.2×10^{-3}	2.2×10^{-3}	2.5×10^{-4}	1.3×10^{-4}	6.1×10^{-3}	7.1×10^{-3}	5.9×10^{-5}	5.4×10^{-5}
ϵ_e	$0.06^{+0.04}_{-0.02}$	$0.21^{+0.07}_{-0.07}$	$0.018^{+0.002}_{-0.002}$	$0.008^{+0.002}_{-0.001}$	$0.046^{+0.011}_{-0.007}$	$0.013^{+0.005}_{-0.005}$	$0.05^{+0.02}_{-0.01}$	$0.054^{+0.011}_{-0.006}$	$0.009^{+0.004}_{-0.002}$	$0.009^{+0.005}_{-0.002}$
E_b (TeV)	$0.046^{+0.04}_{-0.016}$	$0.35^{+0.27}_{-0.15}$	$0.003^{+0.002}_{-0.001}$	$0.0006^{+0.0003}_{-0.0002}$	$0.086^{+0.03}_{-0.013}$	$0.037^{+0.016}_{-0.009}$	$0.027^{+0.015}_{-0.005}$	$0.027^{+0.016}_{-0.004}$	$0.04^{+0.02}_{-0.01}$	$0.05^{+0.02}_{-0.01}$
p	$2.0^{+0.5}_{-0.5}$	$2.4^{+0.4}_{-0.5}$	$1.60^{+0.04}_{-0.04}$	$1.57^{+0.07}_{-0.09}$	$2.16^{+0.05}_{-0.05}$	$2.09^{+0.11}_{-0.11}$	$1.9^{+0.1}_{-0.1}$	$1.9^{+0.1}_{-0.1}$	$2.07^{+0.15}_{-0.08}$	$2.04^{+0.15}_{-0.07}$
E_c (TeV)	15^{+20}_{-11}	21^{+26}_{-7}	6^{+5}_{-3}	2^{+6}_{-1}	32^{+12}_{-12}	37^{+20}_{-09}	16^{+4}_{-2}	17^{+3}_{-2}	$15.2^{+3}_{-1.7}$	19^{+9}_{-5}
B (G)	$0.10^{+0.02}_{-0.02}$	$0.027^{+0.009}_{-0.007}$	$2.7^{+0.5}_{-0.6}$	$5.7^{+1.8}_{-1.0}$	$0.155^{+0.013}_{-0.02}$	$0.21^{+0.04}_{-0.04}$	$0.16^{+0.07}_{-0.03}$	$0.18^{+0.02}_{-0.02}$	$0.42^{+0.03}_{-0.03}$	$0.35^{+0.06}_{-0.06}$

NAIMA includes a function to calculate the loss of energy due to the interaction of gamma-rays with the extragalactic background light (EBL), although we followed the approach used by M. Barnard et al. (2024) and computed the EBL attenuation using the model of A. Domínguez et al. (2011).

We have employed the MCMC technique (D. Foreman-Mackey et al. 2013) available within NAIMA to fit multiwavelength afterglow spectral energy distribution (SED) for each GRB during a time interval with the most data coverage. The best-fitting model parameters thus obtained are then used to calculate model SEDs in other time intervals. The details of the fitting procedure with initialization of the models, priors on the parameters, and selection process for the model are described in Appendices B1 and B2, respectively.

3 DATA ACQUISITION AND ANALYSIS

We have collected radio, optical, and gamma-ray (MeV–VHE) data for our GRB sample from the published papers, while we have analysed X-ray data from *Swift*-XRT by ourselves. We describe this analysis and the data sets used for modelling in this section.

3.1 *Swift*-XRT data analysis

The *Swift*-XRT observations of GRBs are automatically processed by the UK *Swift* Science Data Center (UKSSDC), which generates light curves, time-averaged spectra, and time-sliced spectra (P. A. Evans et al. 2009).[3] For this study, we focus on the time-sliced spectra to match the time-stamp of the multiwavelength data for the VHE GRBs. Both photon counting (PC) mode and window timing (WT) mode data were considered, ensuring comprehensive temporal coverage. The time-sliced XRT spectra were selected only for intervals coincident with observations in other wavelengths, such as optical, infrared, and radio, to generate precise, multi-epoch SEDs.

The XRT time-sliced spectra were analysed using the XSPEC software (version 12.14.0b) within the HEASOFT package, following standard reduction procedures. To improve the reliability of the spectral analysis, we excluded energy channels below 0.5 keV and above 10 keV, as these are often affected by increased uncertainties and instrumental limitations. The initial steps in the spectral fitting involved loading the source spectra, background spectra, and associated response matrix files (RMFs) and ancillary response files (ARFs). We modelled the XRT spectra using an absorbed power-law model, incorporating both Galactic and intrinsic absorption. For the Galactic absorption, we used the *tbabs* model (J. Wilms, A. Allen & R. McCray 2000), which accounts for absorption due to the Galactic ISM with fixed hydrogen column density values. For the intrinsic absorption (i.e. absorption occurring within the host galaxy of the GRB), we employed the *ztbabs* model (J. Wilms et al. 2000), which allows for redshift-dependent absorption.

Post-fitting, the photon flux and photon index (Γ_i) were extracted from the best-fitting model. These parameters were then used to calculate the unabsorbed energy flux by integrating the flux over the XRT energy range (0.5–10 keV). The energy-averaged flux was calculated with the corresponding 1σ error using XSPEC.

3.2 Multiwavelength afterglow SEDs

We describe multiwavelength SED fitting results for each VHE GRB in this section. See Appendix B for a detailed discussion of

[3] https://www.swift.ac.uk/

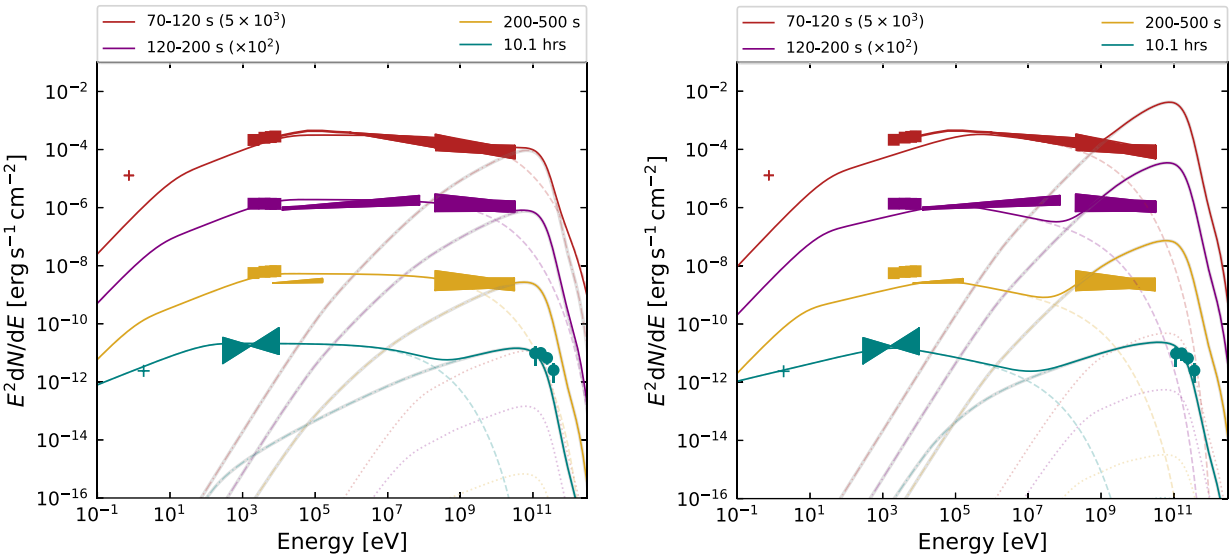

Figure 1. The SEDs for GRB 180720B at several epochs, as indicated in the legend, for the ISM (left) and wind (right) density scenarios. For each epoch the synchrotron (dashed), SSC (dash–dotted), EC (dotted), and total (solid) emission are modelled and fitted to the multiwavelength data, i.e. optical (crosses), *Swift*-XRT (squares), *Swift*-BAT, and *Fermi*-LAT (shaded regions), and H.E.S.S. (circles). For the 10 h epoch the X-ray data is an extrapolation to the time window of the H.E.S.S. observation. The data were collected from M. Sasada et al. (2018), H. Abdalla et al. (2019), N. Fraija et al. (2019), M. Ronchi et al. (2020), and https://www.swift.ac.uk/.

how we have used NAIMA to fit and select the best-fitting model to the multiwavelength observations, as well as the diagnostic plots for each GRB studied in this paper. The results of the best-fitting parameters for each GRB in the case of ISM and wind are compiled in Tables 1 and B1. Since NAIMA does not include a reverse shock component, which could be important during the very early afterglow phase, we do not use data from the epochs that are too close to the prompt emission. Furthermore, we only use spectral data available in the literature for our modelling, and not the light-curve data. This is because conversion of data from light curves to spectra is non-trivial.

3.2.1 GRB 180720B

VHE emission from GRB 180720B was detected approximately 10 h after the initial trigger by the H.E.S.S. telescope (H. Abdalla et al. 2019). This is the only GRB where much-delayed VHE observation was evident. For this epoch the optical and VHE data were sourced from H. Abdalla et al. (2019) and N. Fraija et al. (2019), with the X-ray data an extrapolation to the time window of the H.E.S.S. observation. We obtained the optical, soft X-ray to gamma-ray data for the other epochs from M. Sasada et al. (2018) and M. Ronchi et al. (2020). Multiwavelength SEDs have been constructed for four distinct observational epochs. We have not selected data from very early epochs of GRB 180720B that are too close to the prompt emission. We perform a Bayesian information criterion (BIC) using MCMC for the epoch at 10 h post-burst when H.E.S.S. data were available, for both ISM and wind models. The combination of synchrotron, SSC, and EC is taken into consideration to model the multiwavelength data and the EC contribution was found to be negligible. Based on the SED fitting and corner plots as shown in Figs B1–B4, as well as the multi-epoch SED shown in Fig. 1, we found the ISM model as the better fit. The best-fitting values of model parameters and BIC numbers for both the mediums are tabulated in Tables 1 and B1, respectively. We translated the value of the B-field for other epochs, by calculating the ratio between a given B-field energy and shock energy ϵ_B given in equation (A5), by keeping other model parameters fixed.

At a $z = 0.653$ (P. M. Vreeswijk et al. 2018), GRB 180720B is a highly energetic event, with an isotropic-equivalent energy release of $E_{\rm k,iso} \approx 6 \times 10^{53}$ and 1×10^{54} erg for the ISM and wind cases, respectively. The Γ_0, using $t_{\rm dec} \equiv T_p = 78$ s (M. Ronchi et al. 2020) is larger for the ISM case. GRB 180720B displays afterglow characteristics closely aligned with those of GRB 190114C, except having low number density for the ISM medium, indicating possible similarities between the burst environment and dynamics.

3.2.2 GRB 190114C

GRB 190114C was the first GRB to have VHE photons detected by the MAGIC telescope, with the detection occurring around 60 s post-trigger (MAGIC Collaboration 2019b). VHE data for GRB 190114C was collected for five different epochs, spanning from 68 to 2400 s after the trigger. Furthermore, we also acquired late-time optical and X-ray data from MAGIC Collaboration (2019b) to obtain better constraint on the models. In case of GRB 190114C, we have not included late-time radio or optical data from K. Misra et al. (2021) in our modelling because those data are given only in light curves. The multi-epoch SEDs of GRB 190114C are shown in Fig. 2 for ISM and wind mediums, respectively. A total of 10 epochs were used for the SED modelling. Among them are five time bins that have VHE data, and the rest have late-time optical to X-ray data coverage. The VHE data presented in the study are the observed data before internal and EBL absorption corrections. We selected the second epoch (110–180 s) to run the MCMC sampler because of its good data coverage from X-ray to VHE. After fitting, we obtain our best-fitting parameters for both the ISM and wind mediums, as tabulated in Table 1 and the posterior distributions are shown in Figs B7 and B8. Among the model parameters, the B-field is the only time-dependent parameter. Similar techniques are used to translate parameters for all

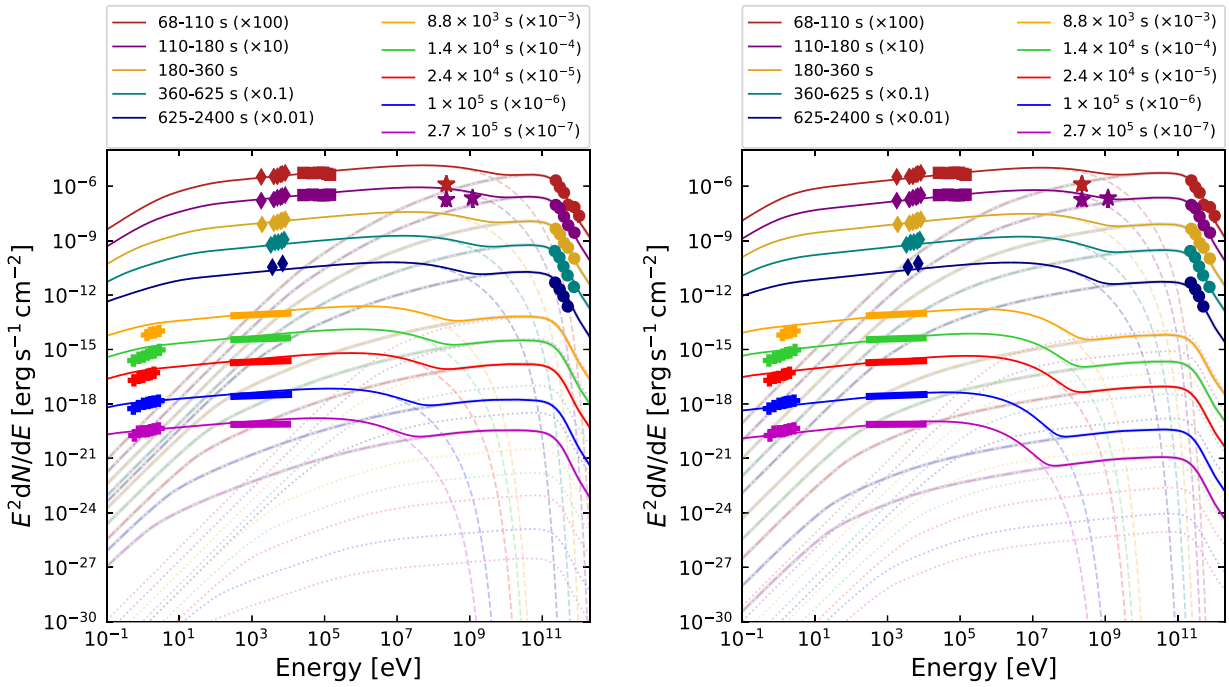

Figure 2. The SEDs for GRB 190114C at several epochs, as indicated in the legend, for both the ISM (left) and wind (right) density scenarios. For each epoch the synchrotron (dashed), SSC (dash–dotted), EC (dotted), and total (solid) emission are modelled and fitted to the multiwavelength data, i.e. optical (crosses), *Swift*-XRT (diamonds and shaded regions), *Swift*-BAT (squares), *Fermi*-LAT (stars), and MAGIC (circles). The data were collected from MAGIC Collaboration (2019b) and https://www.swift.ac.uk/.

the epochs as mentioned in Section 3.2.1 for GRB 180720B. As GRB 190114C occurred at $z = 0.45$ (A. J. Castro-Tirado et al. 2019; J. Selsing et al. 2019), flux attenuation due to the EBL is much higher than the internal $\gamma\gamma$ absorption.

From Table 1, it is evident that GRB 190114C is very energetic ($E_{\rm k,iso} = 8 \times 10^{53}$ erg) and occurred in a denser ISM ($n_0 = 5\,{\rm cm}^{-3}$). We calculated $\Gamma_0 = 167$ and 107 for the ISM and wind, respectively using $t_{\rm dec} \equiv T_{90} = 116$ s (M. Ajello et al. 2020). The optical to VHE data from early to later epochs are well fitted with both the ISM and wind models. From Figs B5–B8, and the composite SED shown in Fig. 2, it is hard to distinguish which model is preferred. However, the BIC values recorded in Table B1 clearly indicates preference for the wind case, even though the high-energy cut-off of the electron distribution E_c is not properly constrained.

3.2.3 *GRB 190829A*

GRB 190829A, the lowest luminosity VHE detected GRB to date, occurred at a relatively lower $z = 0.0785$ (A. F. Valeev et al. 2019). VHE data for two distinct epochs, corresponding to 5 and 30 h (i.e. 0.21 and 1.25 d, respectively) after the GRB trigger, were extracted from H. Abdalla et al. (2021), as illustrated in Fig. 3. The optical and radio observations for these two epochs were obtained from T. Laskar et al. (2019), A. Ugarte Postigo et al. (2019), L. Rhodes et al. (2020), Y. D. Hu et al. (2021), and O. S. Salafia et al. (2022), while the optical and radio data for the remaining epochs were sourced from Y. D. Hu et al. (2021). The SED of GRB 190829A was constructed across multiple epochs from 0.21 to 14.3 d since the burst, whereas the MCMC sampling was performed for the first epoch (0.21 d) because of its robust and simultaneous data coverage across multiple wavelengths. Same models and mediums were used to fit GRB 190829A data like the other two GRBs. Due to the proximity of GRB 190829A, the absorption in EBL was significantly lower than that seen in other VHE GRBs. The ISM model is the more suitable fit over wind because the wind model underpredicts the XRT data as shown in Figs B9 and B10. The best-fitting parameters for the ISM and wind scenarios, along with the corresponding posterior distributions, are presented in Table 1 and B1, and in Figs B11 and B12. For the subsequent epochs, the SED fitting was repeated by adjusting only the B-field strength while keeping other parameters fixed.

GRB 190829A stands out as a unique VHE-detected GRB due to its low $E_{\rm k,iso} = 1 \times 10^{52}$ erg and higher $n_0 = 30\,{\rm cm}^{-3}$. Furthermore, GRB 190829A has low Γ_0 values using $t_{\rm dec} \equiv T_{90} = 63$ s (S. Lesage et al. 2019) for the ISM and wind cases, respectively, compared to the other VHE GRBs.

3.2.4 *GRB 201216C*

At a $z = 1.1$ (L. Izzo et al. 2020), GRB 201216C is the most distant GRB to date for which VHE photons were detected by MAGIC in between 56 and 1200 s after the *Swift*-BAT trigger (H. Abe et al. 2024). Simultaneous detection at other wavelengths is unavailable for the latter epoch, but for the other epochs data were acquired from L. Izzo et al. (2020), L. Rhodes et al. (2022), and H. Abe et al. (2024). So we performed MCMC sampling at 56–1224 s SED, where VHE data points are available. Like other GRBs, the contribution of the EC is negligible compared to the SSC for GRB 201216C. The best-fitting SEDs and the posterior distributions for both ISM and wind-like environments are presented in Figs 4, B13–B16. These results

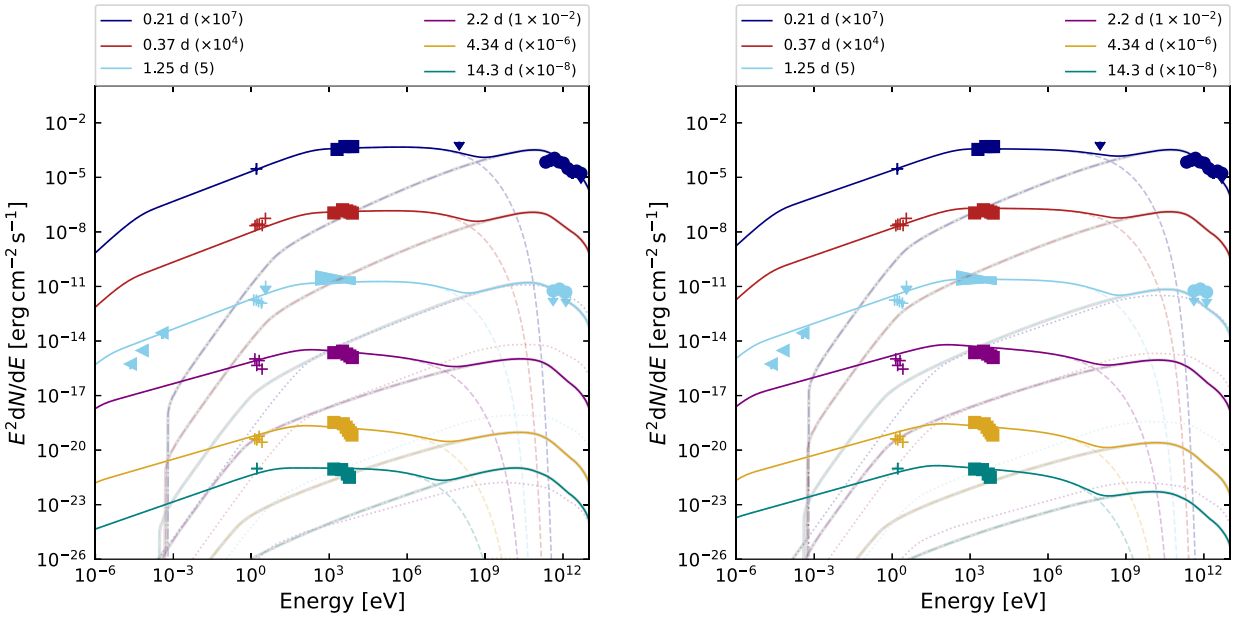

Figure 3. The SEDs for GRB 190829A at several epochs, as indicated in the legend, for the ISM (left) and wind (right) density scenarios. For each epoch the synchrotron (dashed), SSC (dash–dotted), EC (dotted), and total (solid) emission are modelled and fitted to the multiwavelength data, i.e. radio (triangles), optical (crosses), *Swift*-XRT (squares and shaded region), *Fermi*-LAT upper limit, and H.E.S.S. (circles). The data were collected from T. Laskar et al. (2019), A. Ugarte Postigo et al. (2019), L. Rhodes et al. (2020), H. Abdalla et al. (2021), Y. D. Hu et al. (2021), and https://www.swift.ac.uk/.

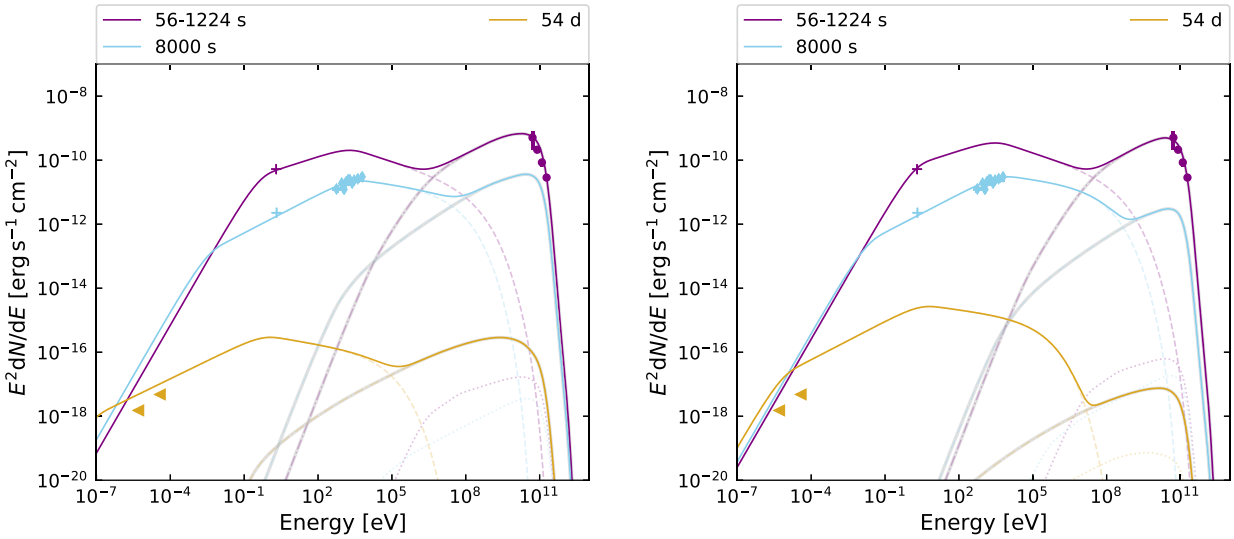

Figure 4. The SEDs for GRB 201216C at several epochs, as indicated in the legend, for the ISM density (left) and the stellar wind (right) scenarios. For each epoch the synchrotron (dashed), SSC (dash–dotted), EC (dotted), and total (solid) emission are modelled and fitted to the multiwavelength data, i.e. radio (triangles), optical (crosses), *Swift*-XRT (diamonds), and MAGIC (circles). The data were collected from L. Izzo, D. B. Malesani & D. A. Kann (2020), L. Rhodes et al. (2022), and H. Abe et al. (2024).

do not allow for a clear distinction between the two circumburst medium scenarios except for the BIC value being lower for the ISM case. The $E_{\rm k,iso} = 6 \times 10^{53}$ erg for both scenarios, although Γ_0 is roughly four times higher for the ISM case, using $t_{\rm dec} \equiv T_p = 60$ s (H. Abe et al. 2024) for both cases respectively. The corresponding best-fitting parameters are summarized in Table 1 and B1.

GRB 201216C shows similar characteristics like those of GRB 190114C and GRB 180720B. Our model overpredicts the late-time radio data for GRB 201216C in both the ISM and wind scenarios.

3.2.5 *GRB 221009A*

GRB 221009A at a $z = 0.151$ (A. J. Castro-Tirado et al. 2022; A. Ugarte Postigo et al. 2022), is recognised as the brightest GRB ever recorded (E. Burns et al. 2023). It exhibited exceptionally high-energy emission, with the detection of up to 18 TeV photons reported by LHASSO (Y. Huang et al. 2022). VHE data for five distinct epochs were obtained from LHAASO Collaboration (2023), while additional multiwavelength data sets across various frequencies were compiled

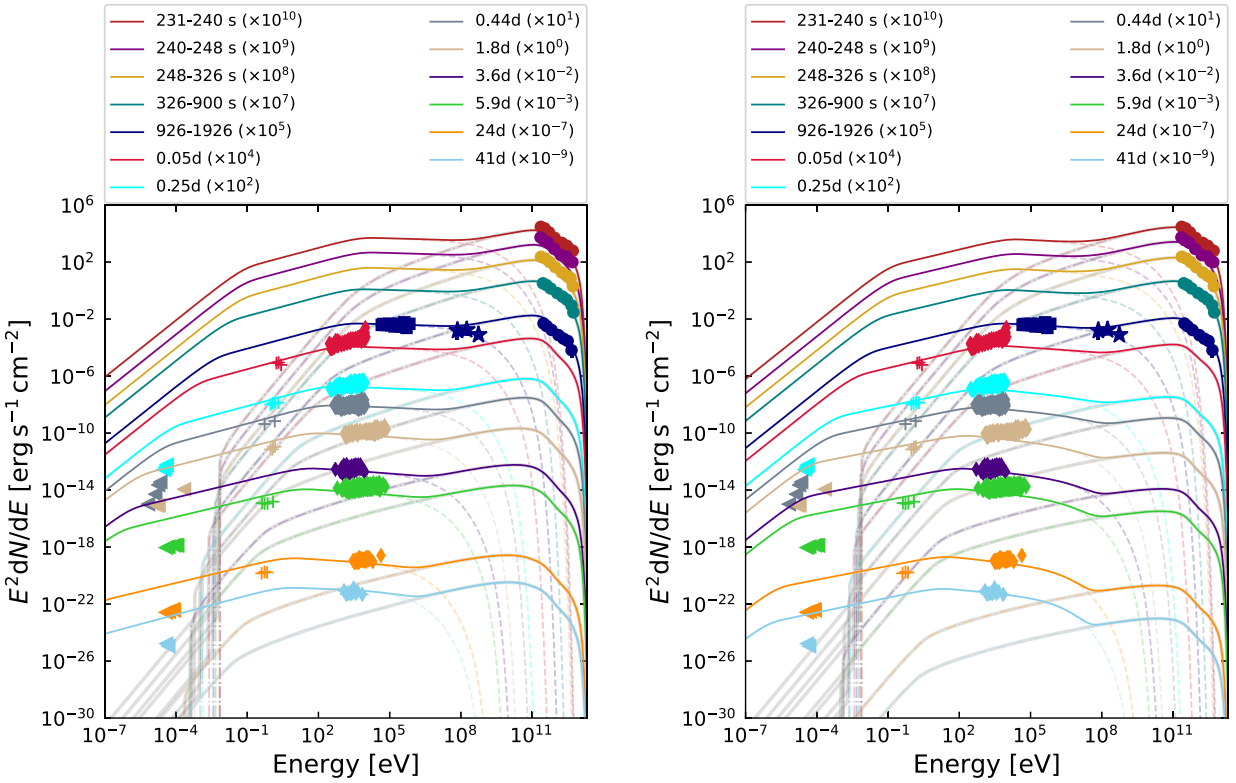

Figure 5. The SEDs for GRB 221009A at several epochs, as indicated in the legend, for the ISM density (left) and the stellar wind (right) scenarios. For each epoch the synchrotron (dashed), SSC (dash–dotted), and total (solid) emission are modelled and fitted to the multiwavelength data, i.e. radio (triangles), optical (crosses), *Swift*-XRT (diamonds), GBM (squares), *AGILE* (stars), and LHAASO (circles). The data were collected from J. S. Bright et al. (2023), LHAASO Collaboration (2023), B. O'Connor et al. (2023), M. Tavani et al. (2023), and B. Banerjee et al. (2024). The EC was omitted for figure clarity.

from both J. S. Bright et al. (2023), B. O'Connor et al. (2023), M. Tavani et al. (2023), and B. Banerjee et al. (2024). The final SEDs were created for 13 different epochs, including the 5 epochs where VHE photons were detected by LHASSO. The MCMC sampling was performed in between 926 and 1926 s since the burst. We have not selected data from very early epochs of GRB 221009A that are too close to the prompt emission. The same model prescriptions were considered for GRB 221009A like the other GRBs, i.e. evolving the B-field by keeping the other parameters fixed for all other epochs. We corrected the VHE data sets with the EBL and internal absorptions. We note that our models overpredicts the late-time radio data in most of the time intervals in both the ISM and wind scenarios.

GRB 221009A was the most energetic burst in our sample, $E_{\rm k,iso} = 1.5 \times 10^{55}$ and 1.2×10^{55} erg, although Γ_0 is rather moderate as mentioned in Table 1, using $t_{\rm dec} \equiv T_p = 230$ s (D. Frederiks et al. 2023) for the ISM and wind cases. The wind medium is preferred over ISM for GRB 221009A based on the BIC values mentioned in Table B1. However, it is challenging to distinguish between the wind and ISM scenarios from the SED fittings and the corner plots shown in Figs 5 and B17–B20.

4 DISCUSSION AND CONCLUSIONS

Since the first detection of VHE photons from GRB 180720B and GRB 190114C, several models have been proposed to date to explain the emission site(s) and radiation mechanism conundrum associated with the VHE GRBs. We discussed some key features of these models below.

(i) First, single-zone analytical models were introduced considering the Thompson and Klein–Nishina cross-sections by E. Derishev & T. Piran (2021) and J. C. Joshi & S. Razzaque (2021). MAGIC Collaboration (2019a) employed a detailed synchrotron and SSC model for ISM medium with EBL correction and Klein–Nishina cross-section to explain the multiwavelength data sets of GRB 190114C.

(ii) O. S. Salafia et al. (2022) used the multizone structured jet model with off-axis scenarios considering both forward and reverse shocks for GRB 190829A. The study by H. Abdalla et al. (2019) tried to fit the multiwavelength SED using the NAIMA code for two epochs during the VHE detection. They only focused on the ISM medium without the cooling constraint. Apart from that they considered two emission models: (1) synchrotron with cut-off + SSC; and (2) synchrotron without cut-off.

(iii) The structure jet morphology with core + wing configuration and their transition was considered by J. Ren et al. (2023) for GRB 221009A. VHE emission in this study was explained by the SSC emission from the core of the jet. In contrast, the low-energy emission comes from forward and reverse shocks of the wing component. B. Banerjee et al. (2024) adopted the leptonic module of LeHaMoC,[4] called LeMoC which covers time-dependent synchrotron + SSC model with self absorption, adiabatic loss consideration, $\gamma\gamma$ pair production and proton–proton inelastic collisions. For the same GRB, Y. Sato et al. (2025) interpreted the multiwavelength afterglow

[4]https://github.com/mariapetro/LeHaMoC

emission using a two-component jet model, comprising two uniform jets with distinct opening angles – one narrow and one wide. They concluded that the narrow jet in GRB 221009A possesses a smaller opening angle, which accounts for its exceptionally large isotropic-equivalent energy.

Aforementioned studies of VHE GRBs have mostly focused on individual events, each analysed with distinct modelling approaches. As a result, direct comparisons among model parameters and population insights have remained pending. Throughout our work, we adopt a unified modelling framework applied consistently to the current sample of VHE detected long-durations. This approach not only ensures a methodological coherence but also enables a population study. Our aim is to study the correlations among the model parameters of VHE GRBs and compare them with the larger sample of long-duration GRBs, offering new insights into their physical properties and emission mechanisms. In our study, we performed a comprehensive multi-epoch panchromatic SED modelling of VHE GRBs using the NAIMA code for a one-zone emission site. NAIMA incorporates the simple approach with the combination of synchrotron and IC emission in the forward shock regime for both the ISM and wind environments. It is a time-independent code that deals with the full Klein–Nishina cross-section and the Bayesian-based MCMC optimization, which is explained in detail in Appendices A and B. We also implemented the EBL correction following A. Domínguez et al. (2011) in the NAIMA code.

In this work, we use multiwavelength data sets of VHE GRBs which are provided in SEDs in the literature. Combining the model with the multiwavelength data sets, spanning from radio to VHE gamma-rays, we constrained five model parameters (the fraction of shock energy transferred to the particles ϵ_e, break energy in electron distribution E_b, E_c, electron spectral index p, and shock B-field) via MCMC optimization. Table 1 shows the best-fitting values of these parameters together with parameters ($E_{\rm k,iso}$, $t_{\rm dec}$, mass-loss rate $\dot{M}_w$, wind speed v_w, A_*, and n_0) that were kept fixed or derived (Γ_0 and ϵ_B) from other parameters. Three GRBs, i.e. GRB 180720B, GRB 190829A, and GRB 201216C, in our sample favour an ISM environment, while the two bright GRBs, i.e. GRB 190114C and GRB 221009A, favour a wind-like profile. Among the VHE-detected long-durations, GRB 180720B, GRB 190114C, and GRB 201216C have comparable isotropic equivalent energies ($\sim 10^{54}$ erg). In contrast, GRB 221009A stands out as the most energetic burst in the sample, while GRB 190829A represents the least energetic event. One common trend found among all the VHE detected GRBs is the low B-field strength and ϵ_B, although with values within the typical range ($\sim 10^{-6}$–10^{-2}) reported in afterglow studies of other long-duration GRBs (R. Santana, R. Barniol Duran & P. Kumar 2014; T. Laskar et al. 2016; M. D. Aksulu et al. 2022). GRB 221009A exhibits the lowest ϵ_B value for the wind medium suggesting a highly inefficient B-field amplification in the shocked circumburst medium. Such low ϵ_B values enhance the SSC contribution, which in turn provide a natural explanation for the observed VHE emission (X.-Y. Wang et al. 2010; N. e. a. Fraija 2019). The parameter Γ_0 varies widely from ∼30 to 370 without exhibiting any trend, however, the ISM medium in general requires higher Γ_0 values compared to the wind medium. VHE GRBs except for GRB 180720B and 201216C, occurred in denser ambient medium. The inferred mass-loss rates from the progenitor stars, in the wind scenario, are consistent across the VHE GRB sample, with GRB 221009A exhibiting the highest value, indicative of a dense stellar wind environment.

Finally, we have investigated the correlation between the $E_{\rm k,iso}$ and ϵ_B across a sample of VHE GRBs and compare with other high-energy GRBs. This high-energy GRB sample was acquired from S. B. Cenko et al. (2010) and M. D. Aksulu et al. (2022). Our analysis reveals a statistically significant anticorrelation between these two parameters, with a Pearson correlation coefficient $r = -0.584$ and a p-value of 5.4×10^{-3}. This trend is depicted in Fig. 6, where the shaded regions represent the 1σ and 3σ confidence interval around the trend-line represented as

$$\log_{10}(E_{k,\rm iso}/\rm erg) = -0.228\ \log_{10}(\epsilon_B) + 52.718\,. \quad (1)$$

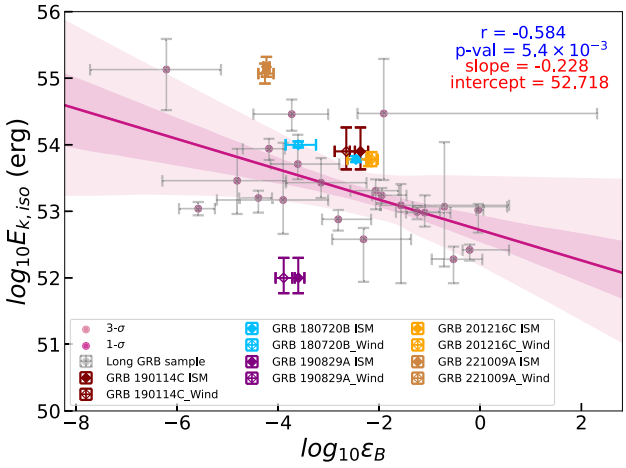

Figure 6. Correlation plot between ϵ_B and $E_{\rm k,iso}$, for the high energetic GRB sample. The diamonds and circles represent VHE detected long-durations and other high energetic long-durations mentioned in S. B. Cenko et al. (2010) and M. D. Aksulu et al. (2022). The shaded regions represent 3σ and 1σ confidence interval, respectively.

Although most VHE GRBs are intrinsically very energetic and lie above the trend-line, they do not follow the trend of other energetic GRBs, falling outside the 3σ confidence region – except for the wind model values of GRB 180720B, which is at the edge. This deviation suggests that VHE GRBs may have a distinct origin or underlying physical mechanism. An exception is GRB 190829A, a lower luminosity GRB, which, as expected, does not fall within this plane, underscoring its unique position among the VHE GRB population.

In conclusion, we find that a single-zone forward-shock model can adequately fit optical to VHE gamma-ray data for all the VHE GRBs in most of the epochs. Our modelling overpredicts the radio flux in the earlier epochs of GRB 190829A, and the later epochs of GRB 201216C and GRB 221009A, when data are available. For GRB 190114C, our modelling can adequately fit optical to VHE gamma-ray data in all epochs, except for the *Fermi*-LAT data during the earliest epoch. Deviation from a single-zone synchro-Compton scenario that we have explored can include (1) an additional emission component; (2) a more complex jet structure; and (3) a more complex density profile of the surrounding environment; or a combination of these. A larger sample of VHE GRBs in the Cherenkov Telescope Array (CTA)-era (B. S. Acharya et al. 2018) will be crucial in modelling VHE GRBs and to learn in more details the nature of these energetic events.

ACKNOWLEDGEMENTS

We thank Marc Klinger and Lauren Rhodes for useful comments. This research was supported by the National Research Foundation

(NRF) of South Africa through a BRICS Multilateral Grant with number 150504. This work was also supported by the NRF of South Africa through a Post-doctoral Fellowship Grant with number 2205056709.

DATA AVAILABILITY

All data used in this work are publicly available from other papers and the *Swift* website https://www.swift.ac.uk/.

REFERENCES

Abdalla H. et al., 2019, Nature, 575, 464
Abdalla H., et al., 2021, Science, 372, 1081
Abe H. et al., 2024, MNRAS, 527, 5856
Acciari V. A. et al., 2021, ApJ, 908, 90
Acharya B. S. et al., 2018, Science with the Cherenkov Telescope Array. World Scientific Publishing, Singapore
Ackermann M. et al., 2013, ApJS, 209, 11
Aharonian F. A., 2000, New A, 5, 377
Aharonian F. A., 2004, Very High Energy Cosmic Gamma Radiation: A Crucial Window on the Extreme Universe. World Scientific Publishing, Singapore
Aharonian F. A., Atoyan A. M., 1981, Ap&SS, 79, 321
Aharonian F. A., Kelner S. R., Prosekin A. Y., 2010, Phys. Rev. D, 82, 043002
Ajello M. et al., 2019, ApJ, 878, 52
Ajello M. et al., 2020, ApJ, 890, 9
Aksulu M. D., Wijers R. A. M. J., van Eerten H. J., van der Horst A. J., 2022, MNRAS, 511, 2848
Alves Batista R., 2022, preprint (arXiv:2210.12855)
Arimoto M. et al., 2024, Nat. Astron., 8, 134
Atoyan A. M., Aharonian F. A., 1996, MNRAS, 278, 525
Banerjee B. et al., 2024, A&A, 701, A68
Barnard M., Razzaque S., Joshi J. C., 2024, MNRAS, 527, 11893
Berti A., Carosi A., 2022, Galaxies, 10, 67
Blanch O. et al., 2020, GRB Coordinates Network, 28659, 1
Blandford R. D., McKee C. F., 1976, Phys. Fluids, 19, 1130
Bright J. S. et al., 2023, Nat. Astron., 7, 986
Burns E. et al., 2023, ApJ, 946, L31
Cao Z. et al., 2023, Sci. Adv., 9, eadj2778
Castro-Tirado A. J. et al., 2019, GRB Coordinates Network, 23708, 1
Castro-Tirado A. J. et al., 2022, GRB Coordinates Network, 32686, 1
Cenko S. B. et al., 2010, ApJ, 711, 641
Das S., Razzaque S., 2023, Astron. Astrophys., 670, L12
de Ugarte Postigo A. et al., 2019, GRB Coordinates Network, 25589, 1
de Ugarte Postigo A. et al., 2022, GRB Coordinates Network, 32648, 1
Derishev E., Piran T., 2021, ApJ, 923, 135
Dermer C. D., Chiang J., Mitman K. E., 2000, ApJ, 537, 785
Domínguez A. et al., 2011, MNRAS, 410, 2556
Eungwanichayapant A., Aharonian F., 2009, Int. J. Mod. Phys. D, 18, 911
Evans P. A. et al., 2009, MNRAS, 397, 1177
Foreman-Mackey D., 2016, J. Open Source Softw., 1, 24
Foreman-Mackey D., Hogg D. W., Lang D., Goodman J., 2013, PASP, 125, 306
Fraija N. et al., 2019a, ApJ, 883, 162
Fraija N. et al., 2019b, ApJ, 885, 29
Fraija N., Veres P., Beniamini P., Galvan-Gamez A., Metzger B. D., Barniol Duran R., Becerra R. L., 2021, ApJ, 918, 12
Frederiks D. et al., 2023, ApJ, 949, L7
Gehrels N., Razzaque S., 2013, Front. Phys., 8, 661
Gill R., Granot J., 2022, Galaxies, 10, 74
Guarini E., Tamborra I., Bégué D., Rudolph A., 2023, MNRAS, 523, 149
Hu Y. D. et al., 2021, A&A, 646, A50
Huang Y., Hu S., Chen S., Zha M., Liu C., Yao Z., Cao Z., Experiment T. L., 2022, GRB Coordinates Network, 32677, 1
Israel H., Bégué D., Pe'er A., 2023b, ApJ, 956, 12
Israel H., Pe'er A., Bégué D., 2023a, ApJ, 955, 70
Izzo L., Malesani D. B., Kann D. A., 2020, GRB Coordinates Network, 29066, 1
Joshi J. C., Razzaque S., 2021, MNRAS, 505, 1718
Khangulyan D., Aharonian F. A., Kelner S. R., 2014, ApJ, 783, 100
Khangulyan D., Taylor A. M., Aharonian F., 2023, ApJ, 947, 87
Klinger M., Tak D., Taylor A. M., Zhu S. J., 2023, MNRAS, 520, 839
Klinger M., Yuan C., Taylor A. M., Winter W., 2024, ApJ, 977, 242
Kumar P., Zhang B., 2015, Phys. Rep., 561, 1
Laskar T. et al., 2016, ApJ, 833, 88
Laskar T. et al., 2019, GRB Coordinates Network, 25676, 1
Lesage S., Poolakkil S., Fletcher C., Meegan C., Goldstein A., Fermi GBM Team, 2019, GRB Coordinates Network, 25575, 1
LHAASO Collaboration, 2023, Science, 380, 1390
MAGIC Collaboration, 2019a, Nature, 575, 455
MAGIC Collaboration, 2019b, Nature, 575, 459
Mészáros P., 2006, Rep. Prog. Phys., 69, 2259
Miceli D., Nava L., 2022, Galaxies, 10, 66
Mirabal N., 2023, MNRAS, 519, L85
Misra K. et al., 2021, MNRAS, 504, 5685
Nakar E., Ando S., Sari R., 2009, ApJ, 703, 675
O'Connor B. et al., 2023, Sci. Adv., 9, eadi1405
Panaitescu A., Kumar P., 2000, ApJ, 543, 66
Piran T., 2004, Rev. Mod. Phys., 76, 1143
Razzaque S., 2010, ApJ, 724, L109
Razzaque S., Dermer C. D., Finke J. D., 2010, Open Astron., 3, 150
Ren J., Wang Y., Zhang L.-L., Dai Z.-G., 2023, ApJ, 947, 53
Rhodes L. et al., 2020, MNRAS, 496, 3326
Rhodes L., van der Horst A. J., Fender R., Aguilera-Dena D. R., Bright J. S., Vergani S., Williams D. R. A., 2022, MNRAS, 513, 1895
Ronchi M. et al., 2020, A&A, 636, A55
Rybicki G. B., Lightman A. P., 1979, Radiative Processes in Astrophysics. Wiley-VCH, New York
Sahu S., Fortín C. E. L., 2020, ApJ, 895, L41
Sahu S., Valadez Polanco I. A., Rajpoot S., 2022, ApJ, 929, 70
Salafia O. S. et al., 2022, ApJ, 931, L19
Santana R., Barniol Duran R., Kumar P., 2014, ApJ, 785, 29
Sari R., Esin A. A., 2001, ApJ, 548, 787
Sasada M., Nakaoka T., Kawabata M., Uchida N., Yamazaki Y., Kawabata K. S., 2018, GRB Coordinates Network, 22977, 1
Sato Y., Murase K., Ohira Y., Inoue S., Yamazaki R., 2025, J. High Energy Astrophys., 48, 100415
Sato Y., Murase K., Ohira Y., Yamazaki R., 2023b, MNRAS, 522, L56
Sato Y., Obayashi K., Theodre Zhang B., Tanaka S. J., Murase K., Ohira Y., Yamazaki R., 2023a, J. High Energy Astrophys., 37, 51
Sato Y., Obayashi K., Yamazaki R., Murase K., Ohira Y., 2021, MNRAS, 504, 5647
Selsing J., Fynbo J. P. U., Heintz K. E., Watson D., 2019, GRB Coordinates Network, 23695, 1
Tavani M. et al., 2023, ApJ, 956, L23
The LHAASO Collaboration, 2023, Sci. Adv., 9, eadj2778
Totani T., 1998, ApJ, 502, L13
Valeev A. F. et al., 2019, GRB Coordinates Network, 25565, 1
Vreeswijk P. M. et al., 2018, GRB Coordinates Network, 22996, 1
Wang X.-Y., He H.-N., Li Z., Wu X.-F., Dai Z.-G., 2010, ApJ, 712, 1232
Wang X.-Y., Liu R.-Y., Zhang H.-M., Xi S.-Q., Zhang B., 2019, ApJ, 884, 117
Wilms J., Allen A., McCray R., 2000, ApJ, 542, 914
Yamasaki S., Piran T., 2022, MNRAS, 512, 2142
Zabalza V., 2015, preprint (arXiv:1509.03319)
Zhang B. T., Murase K., Ioka K., Song D., Yuan C., Mészáros P., 2023, ApJ, 947, L14
Zhang B. T., Murase K., Veres P., Mészáros P., 2021, ApJ, 920, 55
Zheng J.-H., Wang X.-Y., Liu R.-Y., Zhang B., 2024, ApJ, 966, 141

APPENDIX A: NAIMA AFTERGLOW EMISSION MODEL

We adopted a modified version of the GRB emission code used to analyse the multiwavelength afterglow emission of the H.E.S.S. detection of GRB 190829A (H. Abdalla et al. 2021). We applied this GRB code to fit multiwavelength data at different epochs from several GRBs detected in the VHE range at late times (Section 1), to understand the underlying particle acceleration and the blastwave evolution processes with time and distance.

This code utilizes NAIMA software as a tool to compute the non-thermal emission, i.e. synchrotron, and IC from a homogeneous distribution of relativistic particle populations of electrons and protons, assuming an arbitrary user-defined particle distribution function. These radiation models are subsequently fitted to the observed multi-wavelength spectra using MCMC optimization, yielding probability distribution functions for the best-fitting particle parameters (for more details see Appendix B).

A1 GRB blastwave evolution

This section outlines the fundamental expressions for GRB afterglows and the physical parameters used in the code to model their emission, focusing on the underlying assumptions and calculation methods related to the blastwave environment.

Consider a blastwave propagating into the surrounding medium with an isotropic-equivalent energy $E_{\rm k,iso}$ (in erg), a surrounding material density n, and observed at a time t after the GRB trigger. Two environmental scenarios are considered: (i) a constant-density interstellar medium (ISM), and (ii) a stellar wind environment in which the density follows an R^{-2} dependence on the radius R of the emitting shell. A third possible scenario is an average between the first two scenarios, although not used in this study. Given these initial physical parameters of the blastwave, the Lorentz factor Γ of the forward shock is computed using the formalism of R. D. Blandford & C. F. McKee (1976), in which $\Gamma^2 = E_{\rm iso}/Mc^2$, where M is the mass of the material swept-up by the shock. Depending on the scenario chosen, Γ is determined as follows,

$$\Gamma(t) = \begin{cases} \left(\frac{1}{8}\right)^{3/8} \left(\frac{3E_{\rm iso}}{4\pi n(R) m_p c^2 (ct)^3}\right)^{1/8}; & \text{ISM} \\ \left(\frac{3E_{\rm iso} v_w}{4c^3 t \dot{M}_w}\right)^{1/4}; & \text{wind}, \end{cases} \tag{A1}$$

where $\dot{M}_w$ (in solar mass $M_\odot$ per yr) is the mass-loss rate of the progenitor star in a stellar wind with speed $v_{\rm w}$ (in km s^{-1}). Based on the blastwave dynamics described in R. D. Blandford & C. F. McKee (1976), R is determined by the relation $R = A_0\Gamma^2 ct$, where A_0 is a scenario-dependent constant. Thus,

$$R(t) = \Gamma^2 c\Delta t \times \begin{cases} 8; & \text{ISM} \\ 4; & \text{wind}. \end{cases} \tag{A2}$$

The densities in the two cases can be expressed as functions of R as follows:

$$n(R) = \begin{cases} n_0; & \text{ISM} \\ \frac{\dot{M}_w}{4\pi v_{\rm w} R^2 m_p}; & \text{wind}. \end{cases} \tag{A3}$$

A2 Particle distribution and acceleration

The electron distribution is specified prior to computing the particle emission in the blastwave and is assumed to follow an exponential cut-off broken power law (ECBPL) as implemented in NAIMA, and is expressed as follows:

$$f(E) = e^{-(E/E_c)^\beta} \begin{cases} A_0 (E/E_0)^{-\alpha_1}; & E < E_b \\ A_0 (E_b/E_0)^{\alpha_2-\alpha_1} (E/E_0)^{-\alpha_2}; & E > E_b. \end{cases} \tag{A4}$$

Here, E_c is the cut-off energy, E_0 is the reference energy (chosen as 1 TeV), E_b the break energy, α_1 and α_2 are the spectral indices below and above E_b, and A_0 is the normalization. All these quantities are defined in the shock frame.

To model the electron distribution in NAIMA some physical constraints need to be considered. These include:

(i) *Calculate of the minimum injection energy $E_{\rm min}$:* this minimum energy is not fixed a priori but depends on the fraction of shock energy transferred to the particles, denoted by η_e (equivalent to ϵ_e). Using this parameter, $E_{\rm min}$ can be derived from energy and number conservation integrals over the particle distribution. Assuming the injection spectral index $p_{\rm inj} > 2$ and $E_{\rm min} \ll E_{\rm max}$, the resulting expression relates $E_{\rm min}$ to $\eta_e \Gamma m_p c^2$. To ensure numerical stability during MCMC sampling, the ratio of energy to particle number is computed numerically using the full electron distribution. An iterative method adjusts $E_{\rm min}$, starting from 1 GeV, to bring the ratio close to unity. Typically, a single iteration is sufficient for convergence within a factor of 2, balancing accuracy and computational efficiency.

(ii) *Normalization of the electron distribution:* the free parameter η_e relates to the actual normalization of the distribution. The process begins with calculating the internal energy density of the shocked plasma, given by $w = 2\Gamma^2 n_0 m_p c^2$. Based on the values of α_1 and η_e, the value of $E_{\rm min}$ is determined, and a unit-normalized electron energy distribution is constructed. The total energy density of this unit distribution is then calculated using the integral $T = 1/V \int_{E_{\rm min}}^{E_{\rm max}} E {\rm d}N/{\rm d}E {\rm d}E$, where the volume V is that of a spherical shell $V = 4\pi R^2 (R/(9\Gamma))$ with the numerical factor indicating the width of the shell depending on the environment, e.g. $R/9\Gamma$ (for ISM) or $R/3\Gamma$ (for wind). The actual normalization factor A_0 is then found by scaling the unit-normalized distribution so that its energy density matches the physical energy content, given by $A_0 = \eta_e w/T$. Once A is determined, the electron distribution is fully specified and can be used by NAIMA to compute the resulting radiation.

(iii) *Age of the system:* the age of the system is given by the Lorentz-factor corrected time from trigger, $t'_{\rm cool} = (t - t_0)\Gamma$ where the time has been corrected for the relativistic boost (primed quantities are in the shock frame). This means that the cooling break should be in a position in the spectrum for which the energy of the particles have the same cooling time $t_{\rm cool}$ as the age of the system. For a generic GRB, using these relations can give some constrains on the intensity of the B-field imposing that the cooling time of the electrons at the break is at the same level of the age of the system. This constraint is incorporated into the prior function and can be enabled during initialization by setting the cooling constraint option to *true* (see Appendix B).

(iv) *Calculate the internal absorption:* the code takes into account the $\gamma\gamma$-absorption that affects the emitted high-energy photons when they interact with the synchrotron photons inside the source (internal absorption). To take this effect into account, we need the number density of the target radiation field and the cross section of the absorption process. The number density of the target radiation field $n_{\rm ph}$ is actually already computed by NAIMA when determining the SSC component. The cross-section for the process is the analytical approximation coded in F. A. Aharonian (2004). In this way the optical depth parameter τ is computed (see Section A7). Assuming that the size of the region in which absorption and emission happens is the width of the shell, depending on the scenario. In the code there

are two different implementations for the absorption. The default one takes into account that in the same region we have both emission and absorption, i.e. $F = (F'/\tau)(1 - e^{-\tau})$ where F' indicates the intrinsic flux and F the observed flux (G. B. Rybicki & A. P. Lightman 1979). Alternatively, there is also the implementation of $F = F'e^{-\tau}$. In this study we used the latter one.

Once the electron distribution is determined, the population of electrons in the shocked gas is assumed to be accelerated in the B-field in the shocked region. The ratio between a given B-field energy and shock energy is given as ϵ_B, and is expressed as a function of a given B-field strength as follows:

$$\epsilon_B = \frac{B^2}{16\pi\Gamma^2 n m_p c^2}, \tag{A5}$$

with initial parameters including a temporary amplitude (1 eV^{-1}), initial reference energy (E_0 in TeV), E_b, α_1, α_2, E_c, and the exponential cut-off rapidity $\beta = 1$. Once the ECBPL parameters are defined for a certain energy range with the maximum energy equal to E_c, and after the calculation of the $E_{\rm min}$ as a function of η_e and Γ, the synchrotron emission can be determined (see Section A3). Using this calculated synchrotron emission, a new amplitude as a function of η_e, V where the emission takes place, and shock energy can be calculated and used to compute the total energy in the electron distribution.

A3 Synchrotron radiation

NAIMA accounts for the maximum energy of electrons for synchrotron emission by using the effect of synchrotron burn-off, which is due to the balancing of acceleration and synchrotron losses of electrons in the B-field (in units of Gauss), given by equation (18) from F. A. Aharonian (2000) as

$$E_{c,\rm limit} = \left(\frac{3}{2}\right)^{3/4} \sqrt{\frac{1}{e^3 B}} m_{\rm e}^2 c^4 \eta^{-1/2}; \quad \mathrm{TeV} \tag{A6}$$

with all parameters in the cgs units. Here, the acceleration efficiency parameter η is assumed to be ≥ 1.

The synchrotron cooling time of the electrons with energy E_b (in eV) produced in the B-field follows from equation (1) in F. A. Aharonian (2000):

$$t_{\rm cool} = \frac{6\pi m_{\rm e}^4 c^3}{\sigma_{\rm T} m_{\rm e}^2 E_b B^2 (1+Y)}; \quad \mathrm{s} \tag{A7}$$

with $\sigma_{\rm T}$ the Thomson cross-section in cm and the dimensionless Compton parameter Y. The cut-off characteristic energy of a synchrotron photon at the electron cut-off energy and a specific B-field strength [see equation (3.30) from F. A. Aharonian (2004) adapted for electrons] is given as

$$h\nu_c = \sqrt{\frac{3}{2}} \frac{heBE_c^2}{2\pi m_{\rm e}^3 c^5 (1+Y)}; \quad \mathrm{eV} \tag{A8}$$

with h the Planck constant, and $\nu_{\rm c} = (3/2)\nu_{\rm L}(E/m_{\rm e}c^2)^2$ the characteristic frequency of the synchrotron radiation emitted by an electron, with $\nu_{\rm L} = eB/2\pi m_{\rm e}c$ the Larmor frequency. This cut-off photon energy is then used to determine the synchrotron luminosity $L_{\rm sy}$ (in eV s^{-1}). NAIMA uses a thin shell, spherical approximation to calculate the number density of synchrotron photons in the considered emission region. Therefore, no correction factor is needed (see e.g. A. M. Atoyan & F. A. Aharonian 1996) and thus

$$n_{\rm sy} = \frac{L_{\rm sy}}{4\pi R^2 c} \tag{A9}$$

in eV^{-1} cm^{-3}.

For the assumed electron distribution at a given photon energy, and luminosity distance $D_{\rm L}$ from the source, the spectral component is expressed as follows:

$$\left(\frac{\mathrm{d}N}{\mathrm{d}E}\right)_{\rm sy} = \Gamma^2 \left(\frac{\mathrm{d}N}{\mathrm{d}E}\right)_{\rm sy} = \Gamma^2 \frac{L_{\rm sy}}{4\pi D_{\rm L}^2} \tag{A10}$$

where Γ is equivalent to the Doppler boosting, and the flux is transformed to the blastwave frame.

A4 Synchrotron self-Compton radiation

NAIMA assumes a one-zone model to calculate SSC emission, where the target photon field consists of synchrotron photons with a certain energy range and density, as described in Section A3. The synchrotron photon luminosity $L_{\rm sy}$ is computed over a specified energy range and binning. From this, the synchrotron photon number density $n_{\rm sy}$ is obtained using equation (A9).

For the assumed electron distribution at a given photon energy, and $D_{\rm L}$ from the source, with synchrotron target photon field, the spectral component is expressed as follows:

$$\left(\frac{\mathrm{d}N}{\mathrm{d}E}\right)_{\rm SSC} = \Gamma^2 \left(\frac{\mathrm{d}N}{\mathrm{d}E}\right)_{\rm SSC} = \Gamma^2 \frac{L_{\rm SSC}}{4\pi D_{\rm L}^2}. \tag{A11}$$

A5 External Compton radiation

We implemented the IC for external photon fields including the CMB and the far-infrared (FIR). The seed photon field parameters needed are the photon field considered with the associated temperature and energy density. The EC component is computed in the jet frame for each field and then added together to get the total EC flux. The temperature for the FIR is taken as $30\,\Gamma$ (in K), with an energy density of $0.5\,\Gamma^2$ in (eV cm^{-2}). For the CMB field, we assumed a temperature of $2.72\,\Gamma$ (in K), and its energy density of $0.260\,\Gamma^2$ in (eV cm^{-2}). The total EC flux is included in the model with the other components previously mentioned.

For the assumed electron distribution at a given photon energy, and $D_{\rm L}$ from the source, the spectral component is expressed as follows:

$$\left(\frac{\mathrm{d}N}{\mathrm{d}E}\right)_{\rm EC} = \Gamma^2 \left(\frac{\mathrm{d}N}{\mathrm{d}E}\right)_{\rm EC} = \Gamma^2 \frac{L_{\rm EC}}{4\pi D_{\rm L}^2}. \tag{A12}$$

A6 Modified electron cut-off energy

We have modified NAIMA for the maximum energy for electrons by including losses by synchrotron, SSC, and EC simultaneously. Using the expression for the maximum Lorentz factor of the electron distribution $\gamma_s(t)$ in equation (9) from M. Barnard et al. (2024) and the relation $\gamma = (E_c/m_e c^2) + 1$, we could get an estimate for the maximum energy of the electron distribution E_c (in the blastwave frame) using the following expression:

$$E_c = m_e c^2 \left[\left(\frac{6\pi e}{\phi \sigma_{\rm T} B(t)(1 + Y + \Gamma^2 u_{\rm ext}/u_{\rm B})} \right)^{1/2} - 1 \right] \tag{A13}$$

We used $\phi = 10$ and $Y \approx \sqrt{\epsilon_e/\epsilon_B}$ in the slow-cooling regime. This estimate constrained the prior value range for the E_c discussed in Section A3.

A7 Optical depth for $\gamma\gamma$-absorption

NAIMA uses the $\gamma\gamma$ cross-section averaged over scattering angle, with ϵ_γ and ϵ_0 the gamma-ray photon and target photon energy

respectively in eV units (from equation 5 in A. Eungwanichayapant & F. Aharonian 2009 and F. A. Aharonian 2004), as given by

$$\sigma_{\gamma\gamma} = \frac{3\sigma_{\rm T}}{2s_0^2}\left[\left(s_0 + \tfrac{1}{2}\ln s_0 - \tfrac{1}{6} + \tfrac{1}{2s_0}\right)\ln\left(\sqrt{s_0} + \sqrt{s_0 - 1}\right) - \left(s_0 + \tfrac{4}{9} - \tfrac{1}{9s_0}\right)\sqrt{1 - \tfrac{1}{s_0}}\right] [\rm cm^2] \quad \text{(A14)}$$

where $s_0 = \epsilon_\gamma \epsilon_0$, with $s_0 > 1$ is a mask condition to account for the threshold effect, and the cross section is an approximation good within 3 per cent.

The absorption coefficient K that will then be spatially integrated is $K(\epsilon_\gamma) = \int_{\epsilon_0} \sigma_{\gamma\gamma}(\epsilon_\gamma, \epsilon_0)(\mathrm{d}n/\mathrm{d}\epsilon_0)\mathrm{d}\epsilon_0$, where $\mathbf{d}n/\mathrm{d}\epsilon_0$ is the spectral number distribution of the target photon field (the inner integral of equation 3.24 of F. A. Aharonian 2004 in units of eV^{-1} cm^{-3}). The absorption coefficient as (in units cm^{-1}) is

$$K(\epsilon_\gamma) = \int_{\epsilon_1}^{\epsilon_2} \sigma_{\gamma\gamma}(\epsilon_\gamma, \epsilon_0) n(\epsilon_0)\,. \quad \text{(A15)}$$

The corresponding optical depth for gamma-ray absorption, with the assumption of a homogeneous radiation photon field in a source of size R (in cm; from equation 3.24 of F. A. Aharonian 2004), is as follows:

$$\tau(\epsilon_\gamma) = \int_0^R \int_{\epsilon_1}^{\epsilon_2} \sigma_{\gamma\gamma}(\epsilon_\gamma, \epsilon_0)\, n(\epsilon_0, r)\, \mathrm{d}\epsilon\, \mathrm{d}r = RK(\epsilon_\gamma, R) \quad \text{(A16)}$$

with an additional spatial dependence to equation (A15), $n(\epsilon, R)$ that describes both the spectral and spatial distribution of the target photon field in the source. NAIMA computes the optical depth in a shell of width $R/(9\Gamma)$ after transformation of the gamma-ray energy of the data in the blastwave frame. The energy and density of the target photon fields are chosen to calculate both for the SSC and EC emission.

The SSC emission is corrected for $\gamma\gamma$ absorption and EBL attenuation using the flux component in equation (A11) and the opacity in equation (A16) and Section 2 as follows:

$$\left(\frac{\mathrm{d}N}{\mathrm{d}E}\right)_{\rm SSC} = \left(\frac{\mathrm{d}N}{\mathrm{d}E}\right)_{\rm SSC} \exp^{-\tau_{\gamma\gamma}(\epsilon_\gamma)} \exp^{-\tau_{\rm EBL}(\epsilon_\gamma)} \quad \text{(A17)}$$

The EC emission is corrected similarly as the SSC by using the flux component in equation (A12) and the opacity in equation (A16) and Section 2. The total model after absorption is the summation of the distinct components after corrections.

APPENDIX B: OPTIMAL PARAMETER SPACE

We obtained the optimal parameter space in which the emission models describe the observations the best by using a MCMC fitting routine including a BIC employing the PYTHON package EMCEE as the sampler (D. Foreman-Mackey 2016).

B1 Initialization of the model parameters and priors

The functions take automatically the initialization parameters: $E_{\rm k,iso}$, $n = n_0$ (if ISM case is selected), observational gamma-ray energy $E_{\gamma,\rm iso}$, the duration of the afterglow observation determined by and average using $t_{\rm start}$ and $t_{\rm stop}$, z, scenario (ISM or wind), $\dot{M}_{\rm w}$, $v_{\rm w}$, and prior functions to constrain the model, i.e. *cooling constraint* and *synchrotron limit*, see Appendix A for more details of the model. Other prior model parameters for the model fit include $\eta_{\rm e}$ ($\equiv \epsilon_{\rm e}$), E_b, E_c, α_2, and the B-field. The $\log_{10}$ of all prior parameters are taken except α_2. Then the emission from particles are calculated. The index

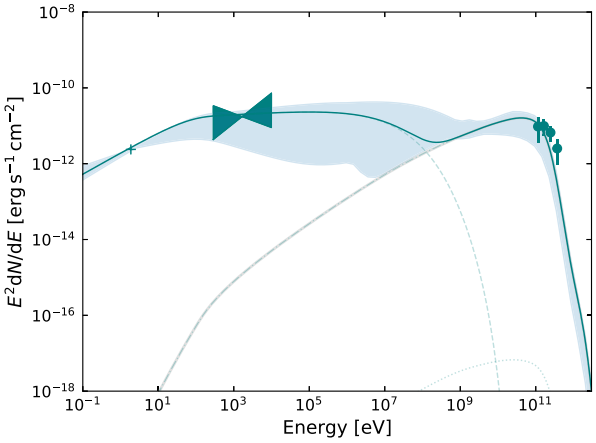

Figure B1. SED fitting of GRB 180720B in the ISM medium. The MCMC 1σ-confidence band is shown over the model for the best-fitting parameters are mentioned in Table 1. The synchrotron (dashed), SSC (dash–dotted), EC (dotted), and total (solid) emission are shown. This line style convention is followed consistently for all VHE GRBs under both the ISM and wind-like ambient medium scenarios.

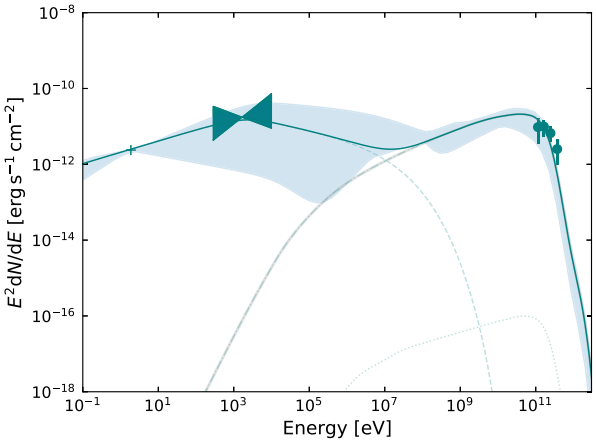

Figure B2. SED fitting of GRB 180720B for the wind medium. The MCMC 1σ-confidence band is shown over the model for the best-fitting parameters are tabulated in Table 1.

α_1 ($= \alpha_2 - 1 \equiv p$) of the electron distribution is fixed to be a cooling break, and α_2 of the electron distribution is free, and the minimum energy and the normalization of the electron distribution are derived from the parameter $\eta_{\rm e}$.

Two constraints that are important when considering the cooling of the synchrotron photons in the system are, the *cooling constraint* that adds to the prior a constraint for which the cooling time at break is approximately the age of the system, and is by default true. The second constraint *synchrotron limit* determines whether the model is synchrotron or IC dominated, thus when false the model is a standard (one-zone) SSC model and if true it is a synchrotron dominated model. The latter constraint is by default false. It is important to note that if the model is synchrotron dominated the *cooling constraint* has no effect.

The basic prior function used is determined by the above constraints, with some basic parameters of the electron distribution left free. The priors are uniformly distributed and take as input the $\log_{10}$ value of the parameters and a lower and an upper limit. The lower

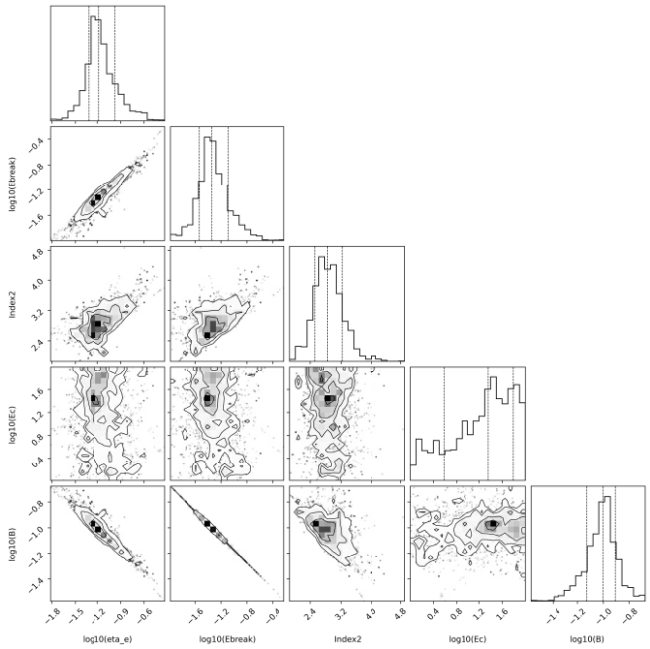

Figure B3. GRB 180720B corner plot for the ISM medium.

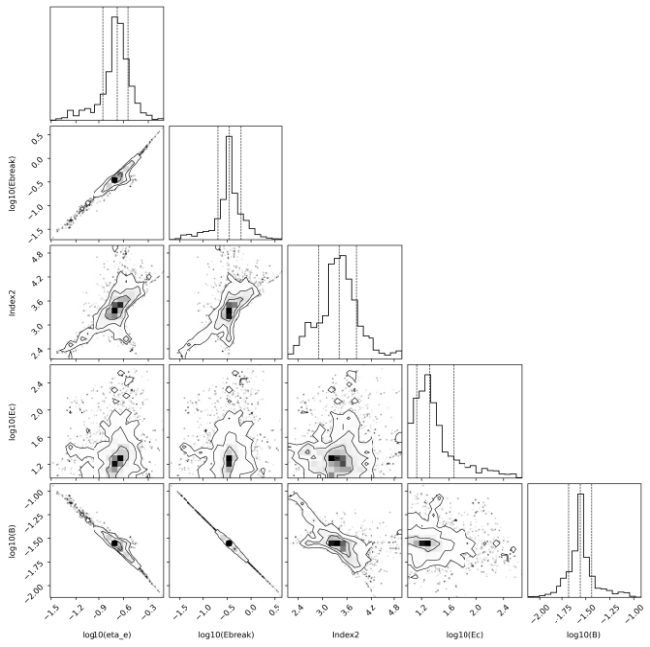

Figure B4. GRB 180720B corner plot for the wind medium.

limit of E_b is the minimum injection energy, and for E_c the upper limit is the maximum limit of the cut-off dictated by the synchrotron burn-off limit; see equation (A6). In this function, the synchrotron cooling time of an electron at the break, to be equal to the co-moving age of the system and is calculated as $t_{\rm age} = \Gamma t$. The cooling time at break energy is calculated using equation (A7) at the given B-field (G) and E_b (TeV). This prior on the cooling time at break (i.e. approximately the age of the system) is implemented through a normal prior distribution which takes the two aforementioned times as inputs, with parameter $t_{\rm cool}$, and the range determined by $t_{\rm age}$.

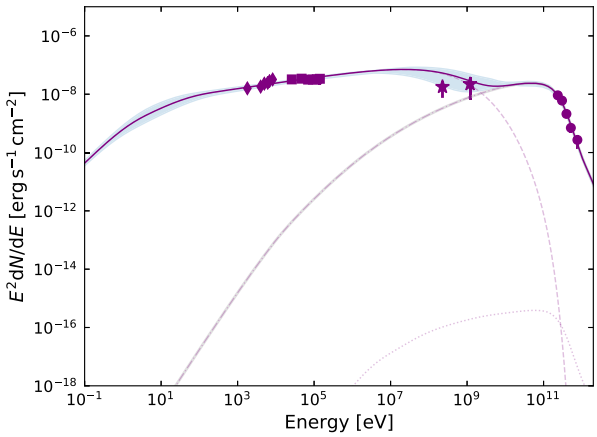

Figure B5. SED fitting of GRB 190114C in the ISM medium. The MCMC 1σ-confidence band is shown over the model for the best-fitting parameters are tabulated in Table 1.

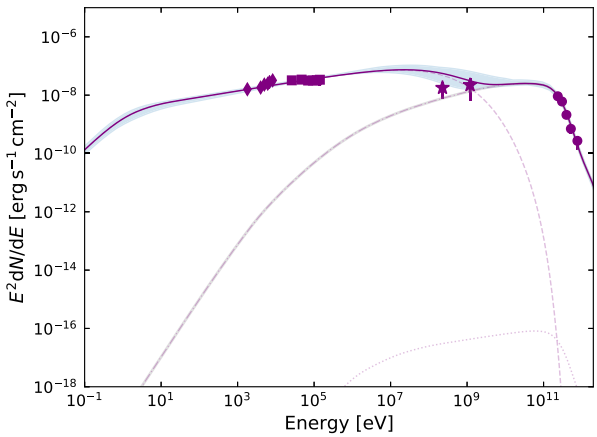

Figure B6. SED fitting of GRB 190114C for the wind medium. The MCMC 1σ-confidence band is shown over the model for the best-fitting parameters are tabulated in Table 1.

Lastly, a prior probability (the sum of all the priors including the additional prior) is returned.

B2 Model fitting and selection of the best fit

The MCMC fitting routine that is used by NAIMA runs the sample (a.k.a. the full chain of the MCMC), save the complete run, and stores the best-fitting results in a table. For each MCMC fitting, the number of parallel walkers, burn-in steps, steps after burn-in, and parallel threads can be chosen. The prefit performs a maximum likelihood (ML) fit to the data set to get a better starting point for the MCMC chain and is by default true. It is important to note that the ML fit might converge in a region not allowed by the parameter space, which is also limited by the lower and upper boundaries set in the prior functions. The fitting routine takes as input the data set, the prior model parameters (see Section B1), the model itself, the probability returned by the prior function, the prefit, the number of walkers, burn-in steps, runs, and threads. After each sample, a set of

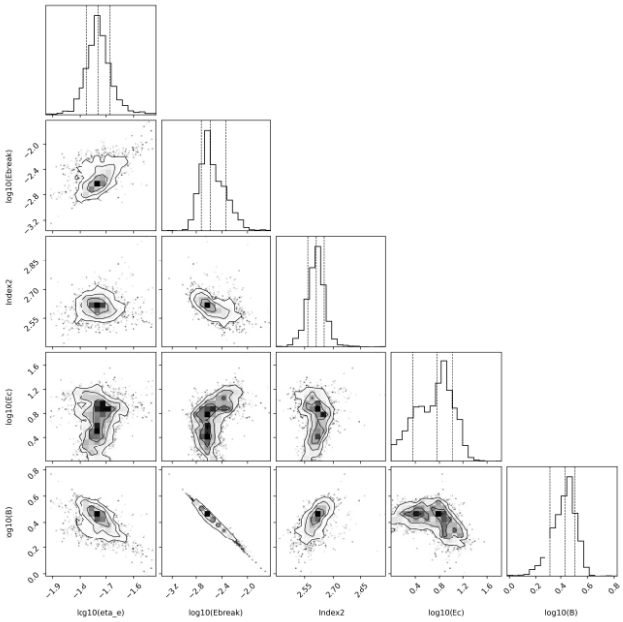

Figure B7. GRB 190114C corner plot for the ISM medium.

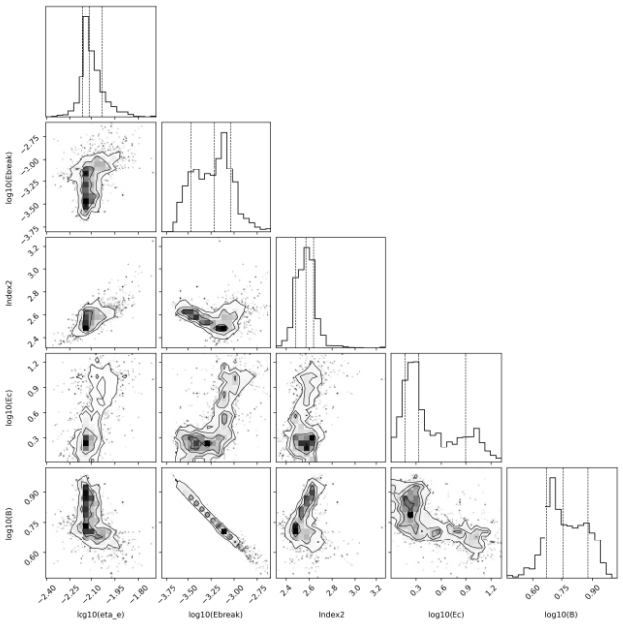

Figure B8. GRB 190114C corner plot for the wind medium.

diagnostic plots is delivered that includes the prior distribution for each model parameter, a corner plot, and the SED that illustrates the model fit to the data and the 1σ-confidence band that corresponds to the corner plot.

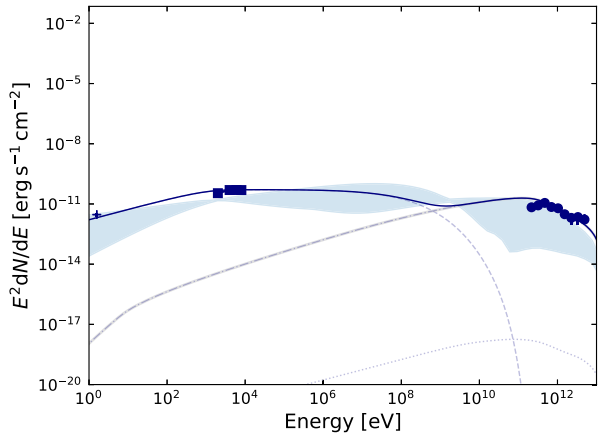

Figure B9. SED fitting of GRB 190829A in the ISM medium. The MCMC 1σ-confidence band is shown over the model for the best-fitting parameters are tabulated in Table 1.

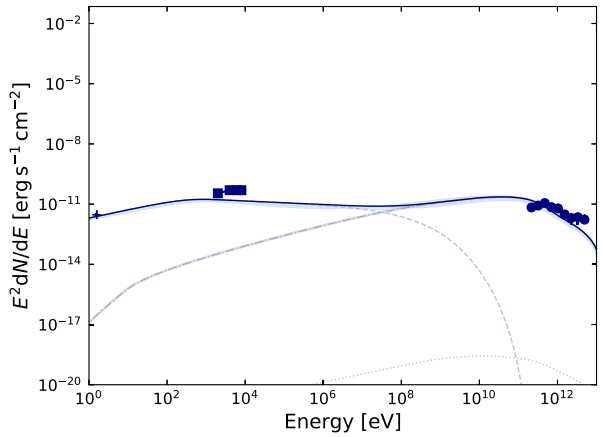

Figure B10. SED fitting of GRB 190829A for the wind medium. The MCMC 1σ-confidence band is shown over the model for the best-fitting parameters are tabulated in Table 1.

The best-fitting model to the data selection is done via the Bayesian inference method through which a given model is selected from a set of possible models. For all competing models, the Bayes factor is computed in order to gauge which model provides a better fit to the multiwavelength data. However, computing the Bayes factor is often non-trivial, and a simpler way to obtain an estimate is using the BIC. Note that the BIC is only a valid approximation for the Bayes factor when the number of data points is much larger than the number of parameters. The BIC is a criterion for model selection among a finite set of models, where models with lower BIC are generally preferred.

The SEDs and corner plots for each GRB studied in the paper are included in this section.

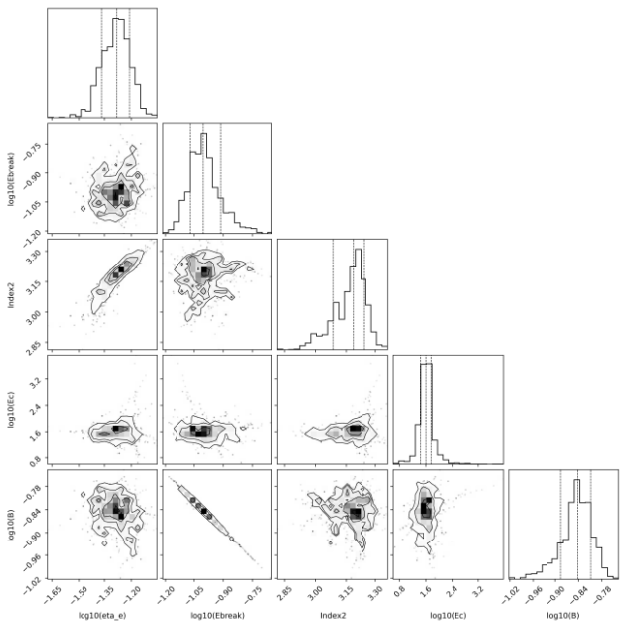

Figure B11. GRB 190829A corner plot for the ISM medium.

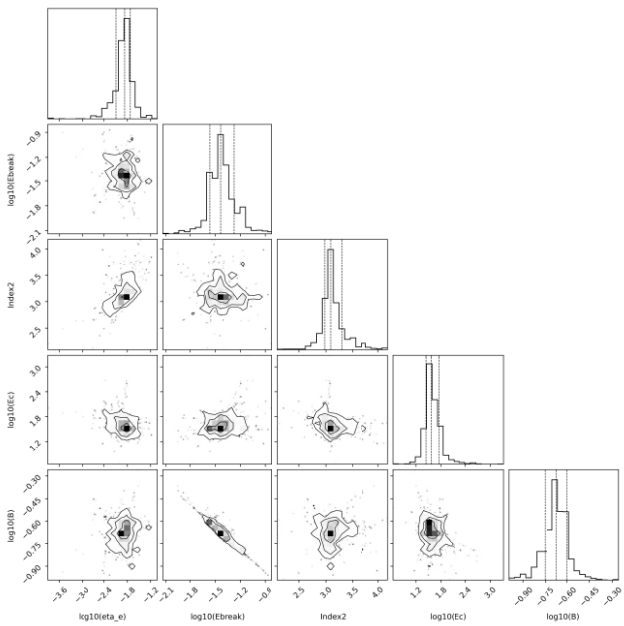

Figure B12. GRB 190829A corner plot for the wind medium.

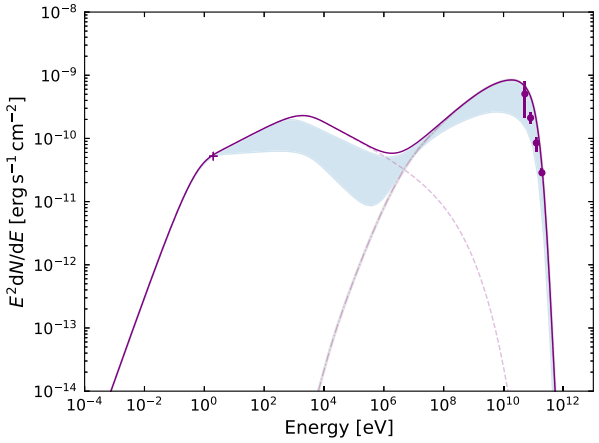

Figure B13. SED fitting of GRB 201216C in the ISM medium. The MCMC 1σ-confidence band is shown over the model for the best-fitting parameters are tabulated in Table 1.

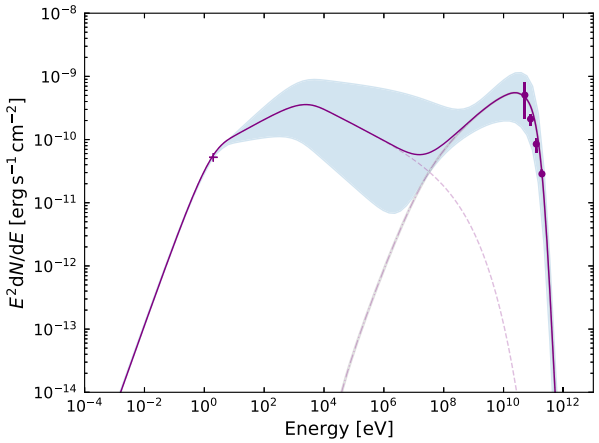

Figure B14. SED fitting of GRB 201216C for the wind medium. The MCMC 1σ-confidence band is shown over the model for the best-fitting parameters are tabulated in Table 1.

Table B1. Comparison of two density scenarios for each GRB. We computed the ΔBIC value to differentiate which fit is better between the competing models, for the same GRB. A lower BIC (bold faced) indicates a better model, and the ΔBIC, calculated by subtracting the best BIC from other models, helps assess the relative quality of those models. The criteria for ΔBIC is as follows based on evidence against the compared model: <2 (negligible), 2–6 (positive), 6–10 (strong), and >10 (very strong).

Source	BIC		ΔBIC
	ISM	Wind	
GRB 180720B	**1382641**	1527916	145275
GRB 190114C	32139	**32011**	128
GRB 190829A	**301846**	375769	73923
GRB 201216C	**241042**	267734	26692
GRB 221009A	778963	**774016**	4947

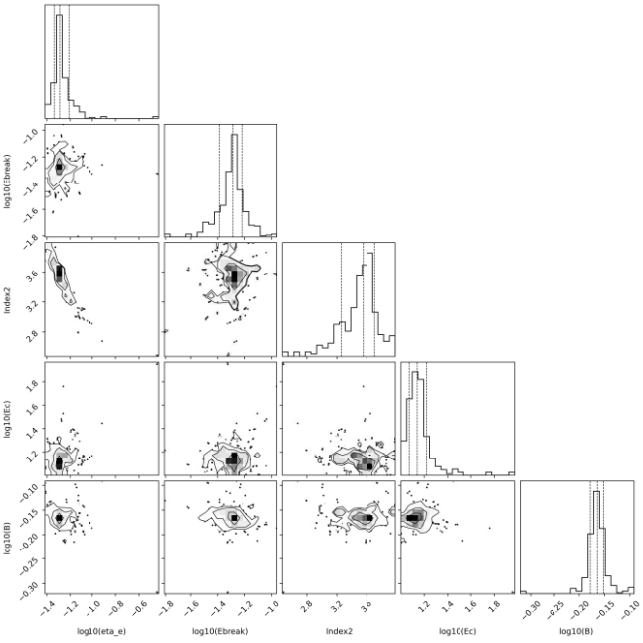

Figure B15. GRB 201216C corner plot for the ISM medium.

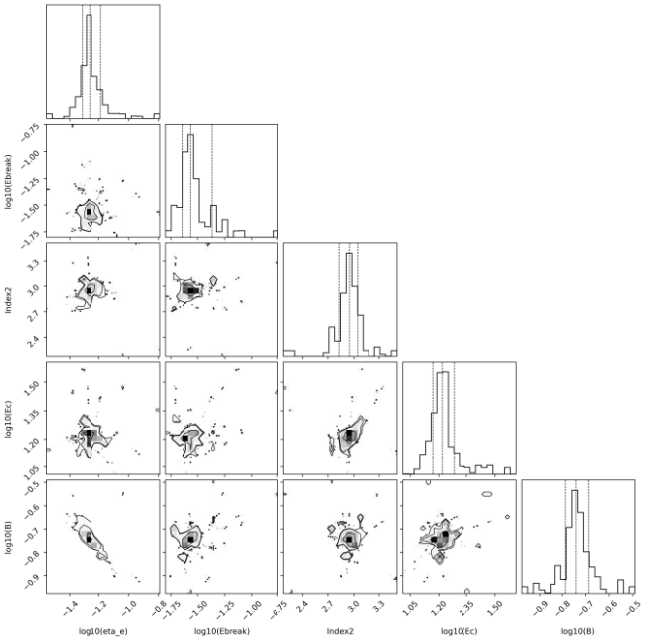

Figure B16. GRB 201216C corner plot for the wind medium.

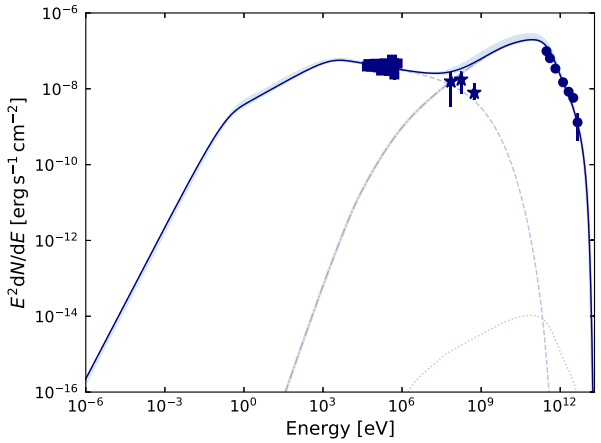

Figure B17. SED fitting of GRB 221009A in the ISM medium. The MCMC 1σ-confidence band is shown over the model for the best-fitting parameters are tabulated in Table 1.

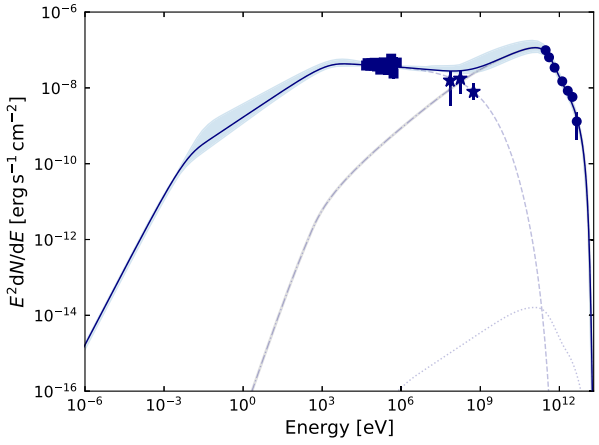

Figure B18. SED fitting of GRB 221009A for the wind medium. The MCMC 1σ-confidence band is shown over the model for the best-fitting parameters are tabulated in Table 1.

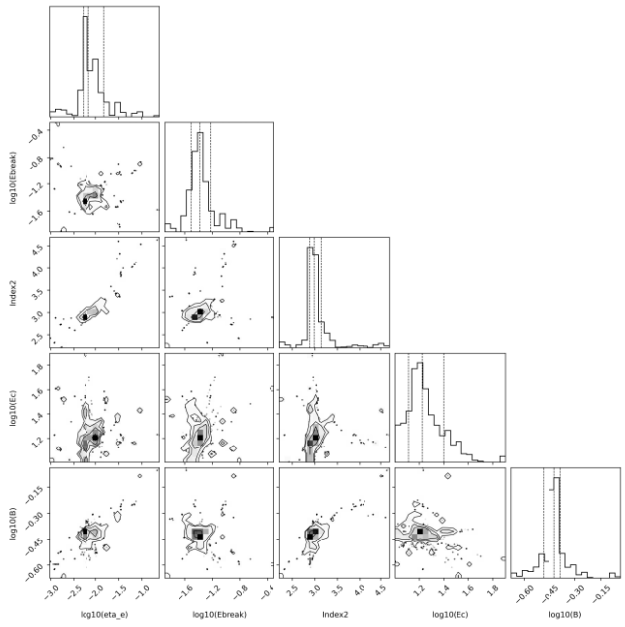

Figure B19. GRB 221009A corner plot for the ISM medium.

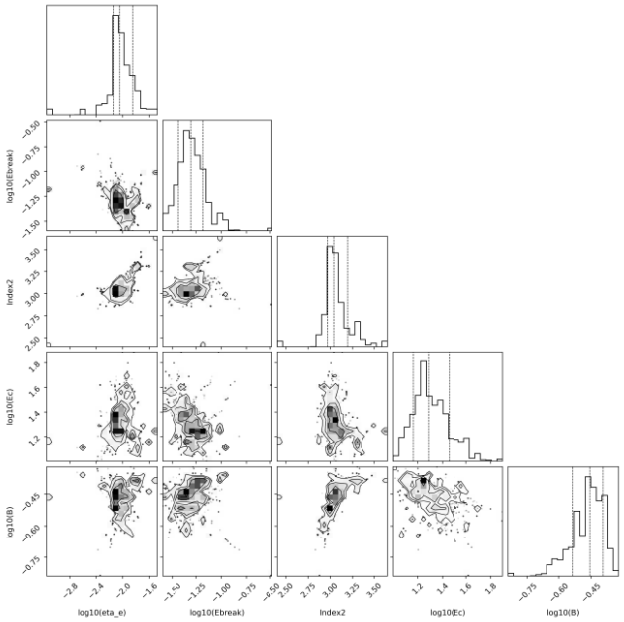

Figure B20. GRB 221009A corner plot for the wind medium.

This paper has been typeset from a TEX/LATEX file prepared by the author.